Article

Not peer-reviewed version

# Post-Collisional Magmatic Evolution of the Castelo Intrusive Complex, Espírito Santo, Brazil: New U-Pb Geochronological Data and Integration of Petrographic and Isotopic Evidence

Iago Mateus Lopes Macedo , Guilherme Loriato Potratz , Marilane Gonzaga Melo , Rodson Abreu Marques , Ana Paula Meyer , Renzo Dias Rodrigues , Marcos Silva Machado , Armando Dias Tavares , Mauro Cesar Geraldes *

Posted Date: 6 November 2024

doi: 10.20944/preprints202411.0370.v1

Keywords: Keywords: Correlation matrix; Zircon U-Pb ages; LA-ICP-MS; Evidences of magma hybridization .

 doi:10.20944/preprints202411.0370.v1



*Article*

# Post-Collisional Magmatic Evolution of the Castelo Intrusive Complex, Espírito Santo, Brazil: New U-Pb Geochronological Data and Integration of Petrographic and Isotopic Evidence

**Iago Mateus Lopes de Macedo [1], Guilherme Loriato Potratz [2], Marilane Gonzaga Melo [3], Rodson de Abreu Marques [4], Ana Paula Meyer [5], Renzo Dias Rodrigues [1], Marco Machado da Silva [1], Armando Dias Taveres [6] and Mauro Cesar Geraldes [2,*]**

[1] Universidade do Estado do Rio de Janeiro, Faculdade de Geologia, Programa de Pós-graduação em Geociências, Rua São Francisco Xavier, 524, Maracanã, Rio de Janeiro, RJ, Brazil.
[2] Universidade do Estado do Rio de Janeiro, Faculdade de Geologia, Departamento de Mineralogia e Petrologia Ígnea, Av. São Francisco Xavier, 524, Maracanã, Rio de Janeiro, RJ, Brazil.
[3] Universidade Federal do Espírito Santo, Departamento de Geologia, Alto Universitário, S/N – Guararema, 29500-000, Alegre, ES, Brazil
[4] Universidade Federal de Ouro Preto, Departamento de Geologia, Morro do Cruzeiro, Ouro Preto, Brazil
[5] Instituto Federal do Espírito Santo, Coordenadoria de Mineração, Cachoeiro de Itapemirim, Brazil
[6] Universidade do Estado do Rio de Janeiro, Instituto de Física, Av. São Francisco Xavier, 524, Maracanã, 20550-013, Rio de Janeiro, RJ, Brazil
* Correspondence: mauro.geraldes@gmail.com

**Abstract:** The Castelo Intrusive Complex (CIC), located in the southern state of Espírito Santo, southeastern Brazil, is a pluton inserted in the context of post-collisional magmatism of the Araçuaí Orogeny, known as Supersuite G5, related to the extensional collapse during the Brasiliano/Pan-African Orogeny. This work presents an integration of field, petrographic, lithogeochemical, and isotopic data, in addition to bringing new U-Pb ages for the CIC and a new geological map. The CIC presents a great compositional variety, presenting rocks of monzogranitic, granodioritic, quartz-monzodioritic, and dioritic compositions that are inserted in the context of mixed magmas. The magma mixing process is generalized in the CIC through field, petrographic, lithogeochemical, and isotopic data, in addition to U-Pb data in the different units that attest to the cogeneticity between them. The delamination process promoted the fusion of the asthenospheric mantle. It promoted the anatexis of different portions of the crust, evident through the values of εHf and TDM ages, where later magmatic mechanisms of physical dispersion (mingling) and chemical diffusion (mixing) favored hybridization and promoted the compositional diversity of the CIC.

**Keywords:** correlation matrix; zircon U-Pb ages; LA-ICP-MS; evidences of magma hybridization

## 1. Introduction

The period of continental collision is marked by intense metamorphism, melting, and continental growth due to crustal accretion [1,2]. Following this period, there is the post-collisional stage, where mafic magmas of mantle origin access the felsic continental crust and can mix, generating different products due to the degree of hybridization and being observed both at the outcrop scale and in thin sections [3–6]. Many authors consider the mixing process as the main mechanism capable of generating compositional variations in suites of igneous rocks [7–9].

Although many authors oppose the mixing process due to the physical difficulties involving contrasting magmas in terms of temperature, viscosity, and degree of crystallinity, among other parameters, the diffusion capacity of the elements allows the mixing mechanism to occur, leading to degrees of homogenization that can be modeled from a geochemical point of view through numerical simulations and experiments [8,9]. In addition, zircon can be used as a powerful petrogenetic tool to

 doi:10.20944/preprints202411.0370.v1



trace magma sources [10,11]. The Araçuaí Orogeny, located in southeastern Brazil and involving the states of Espírito Santo and Minas Gerais, records a long evolutionary history marked by different stages of collision, metamorphism, and magmatism. Intense magmatic activity between 530 and 480 Ma [12,13] marks the post-collisional stage. The rocks generated during this period present a broad compositional spectrum, ranging from gabbro/norite to syenogranite, and several features related to magma mixing [14].

The Castelo Intrusive Complex (CIC) is a representative of post-collisional suite, presenting a wide compositional variation ranging from monzogranite to diorite, exhibiting several features related to magma mixing, and some of its units have recently been studied from a geochronological and isotopic point of view [15]. The objective of this work is to present state-of-the-art research developed in the Castelo Intrusive Complex, present the facies map for the intrusive complex, detail the petrographic characteristics of the rocks that compose it, and present new geochronological data (U-Pb).

## 2. Geological Setting

The Araçuaí Orogeny, together with the Western Congo Orogeny, constitutes an orogenic system developed in the embayment of the São Francisco and Congo paleocontinents during the Brasiliano-Pan-African event, which extended from the Neoproterozoic to the Cambrian-Ordovician boundary, and which resulted in the closure of the Adamastor Ocean and the consolidation of the West Gondwana supercontinent (Figure 1) [16,17], The Araçuaí-Western Congo Orogeny remained united until the opening of the South Atlantic Ocean in the Cretaceous [13,18].

Located in the northern portion of the Mantiqueira Province, the Araçuaí Orogeny is bordered to the north and west by the São Francisco Craton, to the east by the Atlantic Margin, and the south by the Ribeira Orogeny [19,20]. The boundary of the Araçuaí and Ribeira Orogens has been the target of several studies to connect them since no marked discontinuity is observed between them. Instead, a certain continuity is observed between the rocks that compose them, mainly the magmatic arcs, thus forming the Araçuaí-Ribeira Orogenic System (AROS) [20,22–24], proposed an evolution model for the Araçuaí Orogeny known as "nutcracker," divided into five stages: 1) Formation of the precursor Macaúbas basin, 2) Initial convergence stage, 3) Collisional stage, 4) Lateral escape stage of the southern portion, and 5) Gravitational collapse of the Orogeny. Based on a range of field, structural, petrographic, geochemical, geochronological and isotopic data, [12,13] grouped the magmatism of the Araçuaí Orogeny into five supersuites, reflecting different stages of the evolution, known as: G1 (630–580 Ma), G2 (585–540 Ma), G3 (545–500 Ma), G4 and G5 (530–480 Ma).

Supersuite G1 corresponds to the pre-collisional stage, comprising the plutonic arc section. It consists of an expanded calc-alkaline-magnesian series, formed essentially by rocks of granodioritic to tonalitic composition, in addition to mafic enclaves of dioritic composition [13,25–31]. The supracrustal sequences related to the arc are formed by metavolcanosedimentary successions, corresponding to the Rio Doce Group and other related basins, such as the Nova Venécia and Paraíba do Sul Complexes [25,29]. Supersuite G2 comprises the syn-collisional stage and is composed of S-type granitoids, sub-alkaline to alkaline and peraluminous, while supersuite G3 represents the late collisional stage [25,29,32,33]. The post-collisional stage is represented by two super suites, G4 and G5, which consist of calc-alkaline to alkaline granitoids, free from regional deformation [13,14].

Preprints.org (www.preprints.org) | NOT PEER-REVIEWED | Posted: 6 November 2024 doi:10.20944/preprints202411.0370.v1



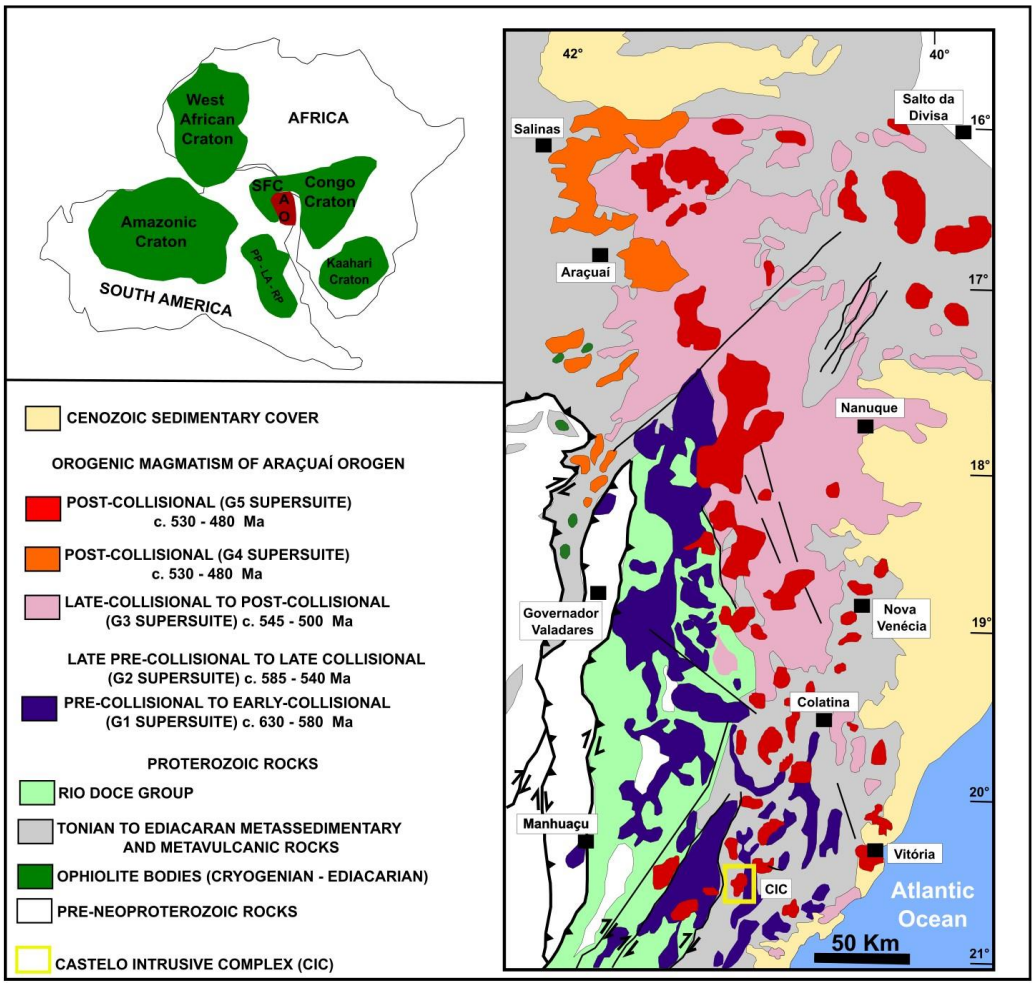


**Figure 1.** Representation of the West Gondwana Supercontinent, delimiting the Araçuaí Orogeny and the adjacent cratonic regions (Modified from [16]). Simplified geological map of the Araçuaí Orogeny (Modified from [13]), showing the study area yellow rectangle).

## 3. Local Geology: G5 Supersuite

Several intrusive bodies mark the post-collisional magmatism of the Araçuaí Orogeny with elliptical, concentric, and oval shapes related to the gravitational collapse of the orogen. These plutons typically have gabbroic/noritic cores surrounded by syenomonzonites, monzonites, and granites and may have external rings of norite and charnockite [13,14,33–39]. The most striking characteristics of these plutons are the absence of regional foliation, evidence of magmatic flow and features related to magma mixing, such as net-veined granitic intrusions, micro granular mafic enclaves and schlieren-like features in granites [15,19,41,42,44–50]. These plutons intrude pre- and syn-collisional granitoids and paragneisses migmatitic (Nova Venécia Complex, Paraíba do Sul, Jequitinhonha). Geothermobarometric data indicate emplacement at shallow crustal levels, showing for the plutons in the southern region of Espírito Santo, such as Pedra Azul, Afonso Cláudio, Santa Angélica, Mimoso do Sul, Venda Nova and Castelo, crystallization at pressures of 5.7 to 11.5 kbar, while the plutons located in the north of the state of Espírito Santo and northeast of Minas Gerais, such as Várzea Alegre, Pedra do Elefante, Barra de São Francisco, Padre Paraíso and Medina, present crystallization at pressures of 2.4 to 3.5 kbar [38,45,46,48,51].

The G5 supersuite magmatism, which corresponds to the last regional event recorded in the Araçuaí Orogeny, is important. This magmatism was triggered by the rise of a hot asthenospheric mantle related to the plate breakup during subduction, followed by a delamination process favoring the crustal anatexis. Isotopic data show a considerable variation for the ratios $^{87}Sr/^{86}Sr$ (0.702–0.741),

 doi:10.20944/preprints202411.0370.v1



$\varepsilon Nd_{(t)}$ (- 3 to - 24), Nd TDM (1.4–2.6 Ga), $\varepsilon Hf_{(t)}$ (+12 to - 24), and Hf TDM ages (1.25–2.4 Ga). Zircon U-Pb ages for the plutons show an age range of 535 to 480 Ma [19,42,43,46,50].

## 4. Materials and Methods

The bibliographic review covered the period from the 1980s, when studies on post-collisional magmatism of the Araçuaí Orogeny began to be published, to the present day. All information regarding the relief, field relationships between the outcropping rocks (and geological maps), airborne geophysical data, petrographic characteristics, and lithogeochemical, isotopic, and geochronological data were compiled for this review.

Fieldwork in the Castelo Intrusive Complex was conducted between 2019 and 2022. During the fieldwork, the contact relationships between the different types of outcropping rocks in the intrusive complex and their relationships with the host rocks were identified, the different plutonic petrographic facies were determined, as defined by [60], and the facies map of the intrusive complex was prepared. In addition to the mapping work, twenty-eight samples (from the intrusive complex) were collected to prepare thin sections and three samples for U-Pb geochronology in zircon grains.

The samples for geochronology were prepared at the Geological Sample Preparation Laboratory (LGPA) of the State University of Rio de Janeiro (UERJ). The samples were then washed, manually reduced using a sledgehammer and anvil, crushed (jaw crusher), and powered (disc mill). The pulverized material underwent density separation processes, starting with the hydrodynamic separation table and followed by separation using dense liquids (iodide and bromoform). Finally, the concentrates underwent magnetic separation (Franz) and manual sorting. After epoxy preparation (fixation of zircon grains to an epoxy resin), the samples are sent to the polishing process of the mount for subsequent imaging in a QUANTA 250 Scanning Electron Microscope (SEM) to produce backscattered and cathodoluminescent images. The SEM image of the zircon grains allows observation of the internal structure of the mineral and evidence of inherited core, areas of reabsorption, and magmatic zoning to guide the subsequent location of the isotopic analysis. The complete description of the sample preparation at Multilab (UERJ-Brazil) is reported by [58].

The U-Pb analyses on zircon grains were performed at the Multi-user Environmental Laboratory (MultiLab) – UERJ, using a Laser-Induced Plasma Mass Spectrometer (LA-ICP-MS) through the Element-2 equipment. The order of data reading in the equipment was: (1) blank reading, (2) reading of the GJ-1 standard, (3) reading of the GJ-1 standard, (4) reading of the 91500 standard, (5) reading of eighteen unknown grains, (6) reading of the blank.

The grain surface was ablated using laser pulses with a diameter of 30 μm. The material vaporized by the laser was transported in Ar (0.80 L/min) and He (0.55 L/min) for analysis using 700 cycles of 1 second each. The analyses included mass measurements of $^{204}Pb$, $^{206}Pb$, $^{207}Pb$, $^{208}Pb$, $^{232}Th$ and $^{238}U$. Hg represents a common contaminant in He and Ar gases, resulting in an isobaric $^{204}Hg$ interference with the $^{204}Pb$ mass. The samples were analyzed together with the zircon reference materials GJ-1 (TIMS normalization data $^{207}Pb/^{206}Pb$ = 608.3 Ma, $^{206}Pb/^{238}U$ = 600.7 Ma and $^{207}Pb/^{235}U$ = 602.2 Ma [59] and the results obtained during this investigation was 608.5 ± 0.4Ma. For reference material 91,500 (TIMS-ID age for $^{206}Pb/^{238}U$ = 1062.4 ± 0.8 Ma and $^{207}Pb/^{206}Pb$ = 1065.4 ± 0.6 Ma, according to [59], and the results obtained here indicate a crystallization age of 1065 ± 6 Ma.

## 5. Results

### *5.1. Castelo Intrusive Complex*

The Castelo Intrusive Complex (Figure 2—Geological Map) generally has an elliptical shape and mountainous relief. However, it has some lowered portions in the southern and central regions of the massif. Outcrops are observed in road cuts, quarries, walls, and waterfalls. Blocks and boulders are common and are associated with the exploitation of dimension stones in quarries. The boundary between the pluton and its host rocks is well-marked by geomorphology.

 doi:10.20944/preprints202411.0370.v1



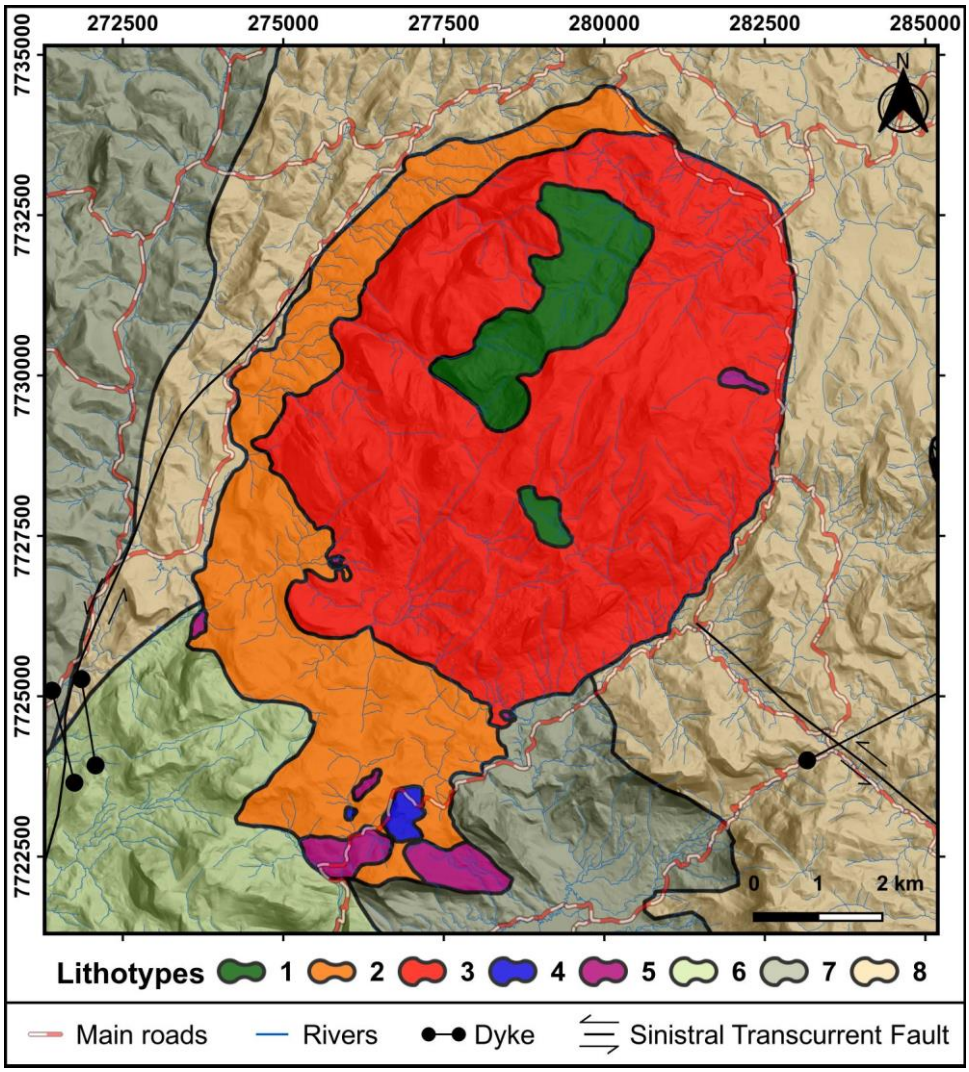


**Figure 2.** CIC geological map. Legend: (1) Diorite; (2) Fine- to coarse-grained inequigranular monzogranite; (3) Porphyritic monzogranite; (4) Granodiorite; (5) Quartz-Monzodiorite; (6) São Fidélis paragneisses; (7) Italva paragneisses; (8) Orthogneiss.

The mapped units in the Castelo Intrusive Complex are (i) Porphyritic monzogranite, (ii) Fine to coarse inequigranular monzogranite, (iii) Granodiorite, (iv) Quartz-monzodiorite, and (v) Diorite (Figure 3) (Table 1). The CIC has a steep sub-vertical escaped relief, forming elongated mountain ranges with rounded tops, mainly in the granite domain outside this domain, where granodiorite, diorite, and quartz-monzodiorite outcrop, and the relief tends to be lower, where the main drainages are located. The topographic contrast between the host rocks and the CIC is that the host rocks are usually presented as gentler mountain ranges, hills, and mountains.

 doi:10.20944/preprints202411.0370.v1



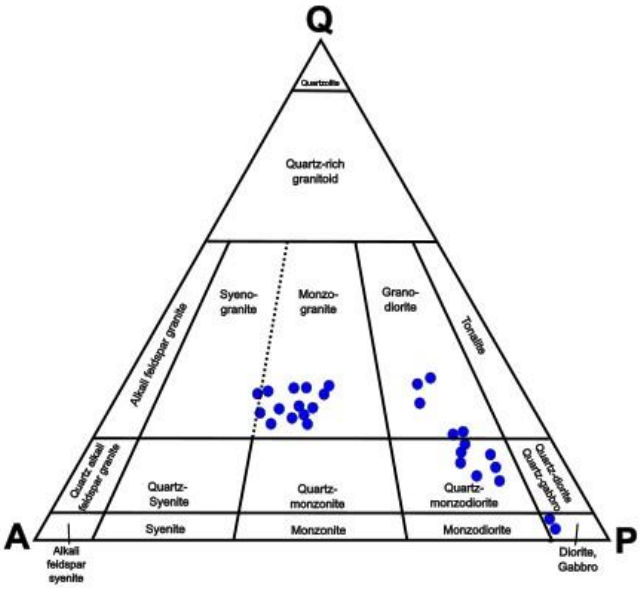


**Figure 3.** QAP diagram for the rocks of the Castelo Intrusive Complex. (Modified from [59]).

**Table 1.** Mineralogical description of all rock types in this study, using the mineral abbreviations of [60].

| Rock Ttype | Main Mineralogy | Accessory Mineralogy |
|---|---|---|
| Monzogranite | Qtz+Kfs+Pl+Bt | Opq+Ttn+Ap+Zrn+Aln+Hbl |
| Granodiorite | Qtz+Kfs+Pl+Bt+Hbl | Opq+Ttn+Ap+Zrn |
| Quartz-Monzodiorite | Qtz+Kfs+Pl+Bt+Hbl | Opq+Ttn+Ap |
| Diorite | Pl+Bt+Hbl | Qtz+Kfs+Opq+Ttn+Ap |

The host rocks of the CIC are (i) biotite gneiss with amphibolite enclaves, (ii) migmatitic paragneiss, and (iii) marble with amphibolite intrusions. Biotite gneiss is the main unit hosting the CIC. It presents discontinuous metamorphic banding, sometimes continuous, spaced millimetrically to centimetrically, consistent with the regional foliation, marked mainly by K-feldspar porphyroblasts in the felsic band and by biotite and amphibole in the mafic band. The migmatitic paragneiss unit presents a gradational contact with the biotite gneiss unit, and its principal characteristic is the features related to migmatization. Marble with amphibolite intrusions occurs in isolated lenses with exploration queries. The main characteristics of this unit are the skarnitization processes and structures, such as concentric folds and boundins.

The monzogranite outcrops are mainly at the edges of the massif (Figure 4 A), presenting only facies variation without compositional change. The edge of the Castelo Intrusive Complex is marked mainly by the fine- to coarse-grained inequigranular monzogranite (Figure 4 B), passing to the porphyritic monzogranite, with K-feldspar phenocrysts of up to 6 cm (Figure 4 C), as it approaches the center of the intrusion. These two facies present micro granular mafic enclaves (Figure 4 D) of different compositions, sizes, and textures, and features analogous to schlieren of various sizes and sometimes oriented.

Mafic dikes are observed occasionally, and syn plutonic mafic dikes with a high degree of hybridization with the host granite are common. Pegmatitic dikes and intrusions of late leucogranites and even mafic rocks are common, generating agmatic features (Figure 4 E). Xenoliths of the host rock are observed in both facies, presenting various sizes and shapes and degrees of assimilation. In the porphyritic facies, the alignment of K-feldspar phenocrysts is joint, indicating igneous flow. The composition of the monzogranite (Figure 5 A to D) of: Microcline (40-30%), plagioclase (30-20%), quartz (35-25%), biotite (25-15%), orthoclase (15-20%), titanite (5%), opaques (5%), allanite (2-5%),

 doi:10.20944/preprints202411.0370.v1



zircon (1%), hornblende (<1%). Muscovite (<1%), sericite (<1%), chlorite (<1%) and carbonates (<1%) are secondary minerals.

Granodiorite is the least common lithotype, occurring punctually in the central-southern portion of the CIC. It is usually gray and often yellowish, with an inequigranular texture and fine to medium grain size (Figure 4 G). It presents small plagioclase xenocrysts, mostly rounded and mafic enclaves. It is common to observe clots of mafic minerals and leucocratic injections of granite in the form of dikes or pockets (Figure 4 F). When the grain size is fine, it usually presents a salt and pepper texture due to the contrast in color between the felsic and mafic minerals. The mineralogy consists of: Quartz (35-25%), plagioclase (35-25%), orthoclase (10-15%), biotite (15-25%), hornblende (15-20%), titanite (5%), opaque minerals (5%), apatite (1-5%), zircon (<1%). Sericite (1%) and chlorite (1%) are secondary minerals. It presents plagioclase crystals evidencing compositional zoning (Figure 5 E and F).

Quartz-monzodiorite is the predominant unit in the mixed zone, often associated with monzogranite, in contact with it, and is predominant in the central-southern portion of the CIC (Figure 4 H). It is dark gray to black in color, meso- to melanocratic, equigranular, and fine-grained (Figure 4 I). Coarse-grained granitic intrusions in the form of veins, pegmatites, and pockets are widespread in interdigitated to abrupt contacts (Figure 4 J). From the interaction between the host quartz-monzodiorite and the granitic intrusions, some features related to magma mixing are found, such as chilled margins, features analogous to pillows, rounded, corroded feldspar xenocrysts, and zones of inclusion of mafic minerals in these xenocrysts, in addition to small mixing zones. The mineralogy consists of plagioclase (40-30%), hornblende (30-20%), biotite (20-10%), quartz (10%), orthoclase (10%), titanite (5%), and opaque minerals and apatite (<5%). From a microscopic point of view, this lithotype presents features indicative of mixing, recorded mainly in the plagioclase, such as compositional zoning (Figure 5 G), plagioclase laths with evidence of corrosion at the edges (Figure 5 H), boxy cellular textures (Figure 5 I) and slots of mafic minerals. Other textures related to magma mixing are apatite crystal mix and poikilitic texture.

The diorite occurs in the core of the CIC, in the topographically lowest region, surrounded by large monzogranite scarps and appearing as large enclaves within them. Several coarse-grained granite dikes and pockets with tabular K-feldspar phenocrysts (Figure 4 K) were cut. The diorite is dark gray in color, melanocratic, equigranular, medium to coarse-grained, and has mafic clots of a few centimeters (~ 3 cm) (Figure 4 L). Its composition consists of hornblende (40-35%), plagioclase (35-30%), biotite (25-20%), quartz (8-5%), orthoclase (5%), apatite (5%), opaques (5%), titanite (5%), and zircon (1%). Biotite, hornblende, and apatite aggregates are common, in addition to quartz xenocrysts, which in some cases are surrounded by hornblende crystals, evidencing the ocellar quartz-hornblende texture (Figure 5 J, K, and L).

 doi:10.20944/preprints202411.0370.v1



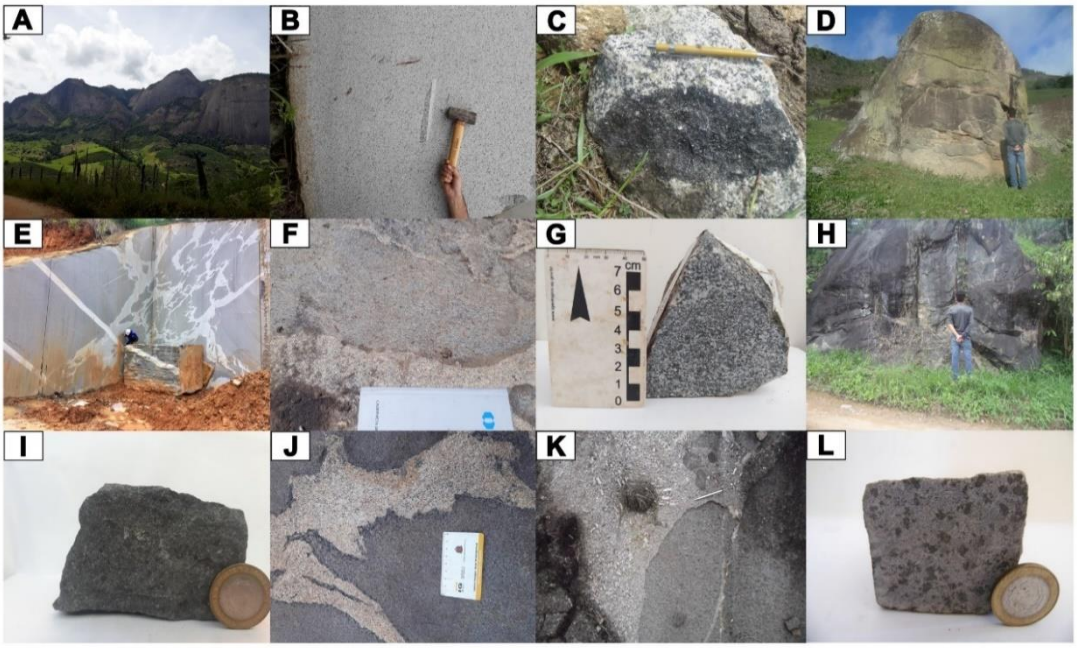


**Figure 4.** A) Topographic contrast between the hills of the country rocks and the steep relief of the CIC, B) Quarry cut of the fine-grained monzogranitic facies, C) Microgranular mafic enclave present in the porphyritic monzogranite, D) Large micro granular mafic enclave in a block of porphyritic monzogranite, E) Agmatic feature observed in a quarry cut at the edge of the CIC, F) Granodiorite outcrop with late granitic intrusion, G) Granodiorite hand sample, H) Quartz-monzodiorite outcrop in the south-central portion of the CIC, I) Quartz-monzodiorite hand sample, J) Quartz-monzodiorite outcrop with granitic intrusion forming cooled margins and hybrid zones, K) Diorite outcrop in the central portion of the CIC, showing granitic intrusions, L) Hand species of diorite.

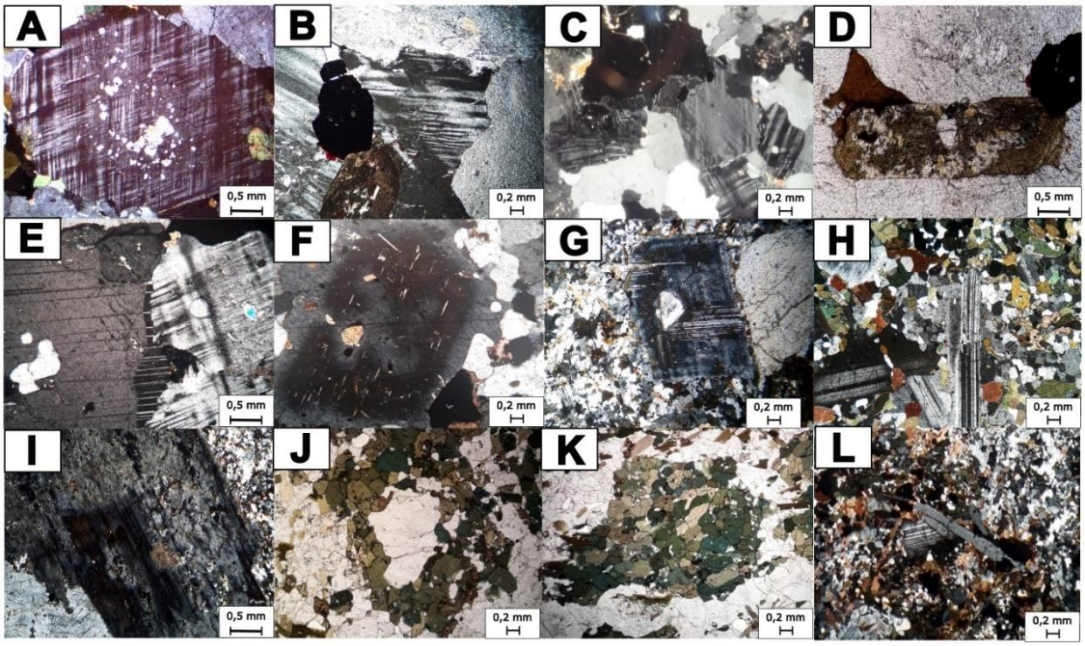


**Figure 5.** A) Poikilitic microcline crystal in monzogranite; B) K-feldspar in monzogranite; C) Quartz and microcline crystals in monzogranite; D) Allanite crystal in monzogranite; E) Syntax texture in plagioclase crystal in granodiorite; F) Zoned plagioclase crystal in granodiorite; G) Zoned plagioclase crystal in quartz-monzodiorite; H) Plagioclase lath with corrosion edges in quartz-monzodiorite; I) Plagioclase crystal showing boxy cellular texture in quartz-monzodiorite; J) Ocellar quartz-hornblende texture in diorite; K) Mafic mineral clots in diorite; L) Mix of apatite crystals in diorite.

 doi:10.20944/preprints202411.0370.v1



*5.2. Lithogeochemical Characteristics*

The lithogeochemical data presented here were compiled from the works of [9,14,62]. The new lithogeochemical data are presented in supplementary material A. Each of the works presents different lithological classifications for the rocks of the CIC. Therefore, we grouped the rocks regarding chemical classification, as observed in the classification diagram R1-R2, adapted from [63] (Figure 6).

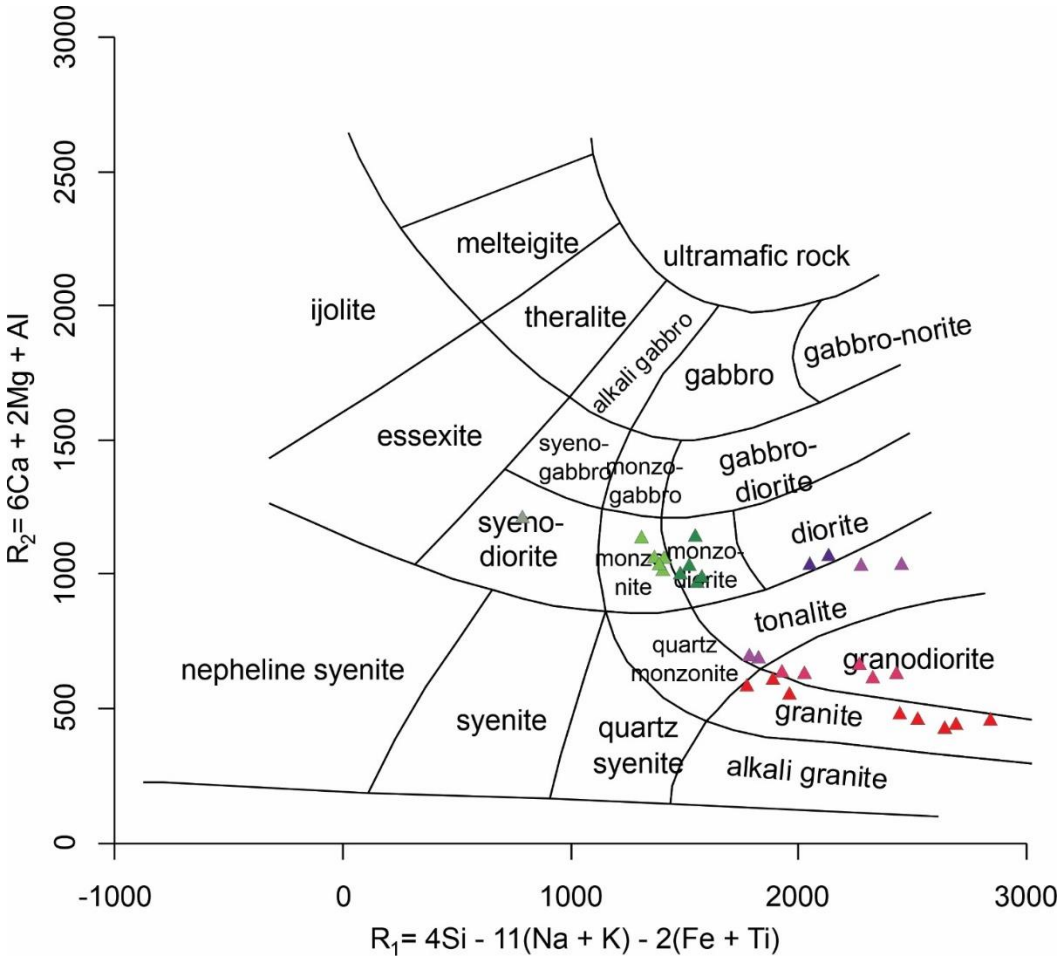


**Figure 6.** Diagram R1-R2, adapted from [63] for the classification of plutonic rocks, where lithogeochemical data of the rocks of the Castelo Intrusive Complex are plotted.

The chemical classification diagram (Figure 6) demonstrates the compositional variation of the rocks of the CIC, where syenodiorite, monzodiorite, monzonite, diorite, tonalite, granodiorite, and granite are present. Another parameter that demonstrates the compositional variability of the rocks of the CIC is the $SiO_2$ content, which varies between 50.19 and 74.14% (Figure 7). Figure 7 shows the behavior of the main oxides concerning the variation in the $SiO_2$ content, where a possible "compositional gap" (3.72%) was observed between 58.17% and 61.89% of $SiO_2$.

Preprints.org (www.preprints.org) | NOT PEER-REVIEWED | Posted: 6 November 2024 doi:10.20944/preprints202411.0370.v1



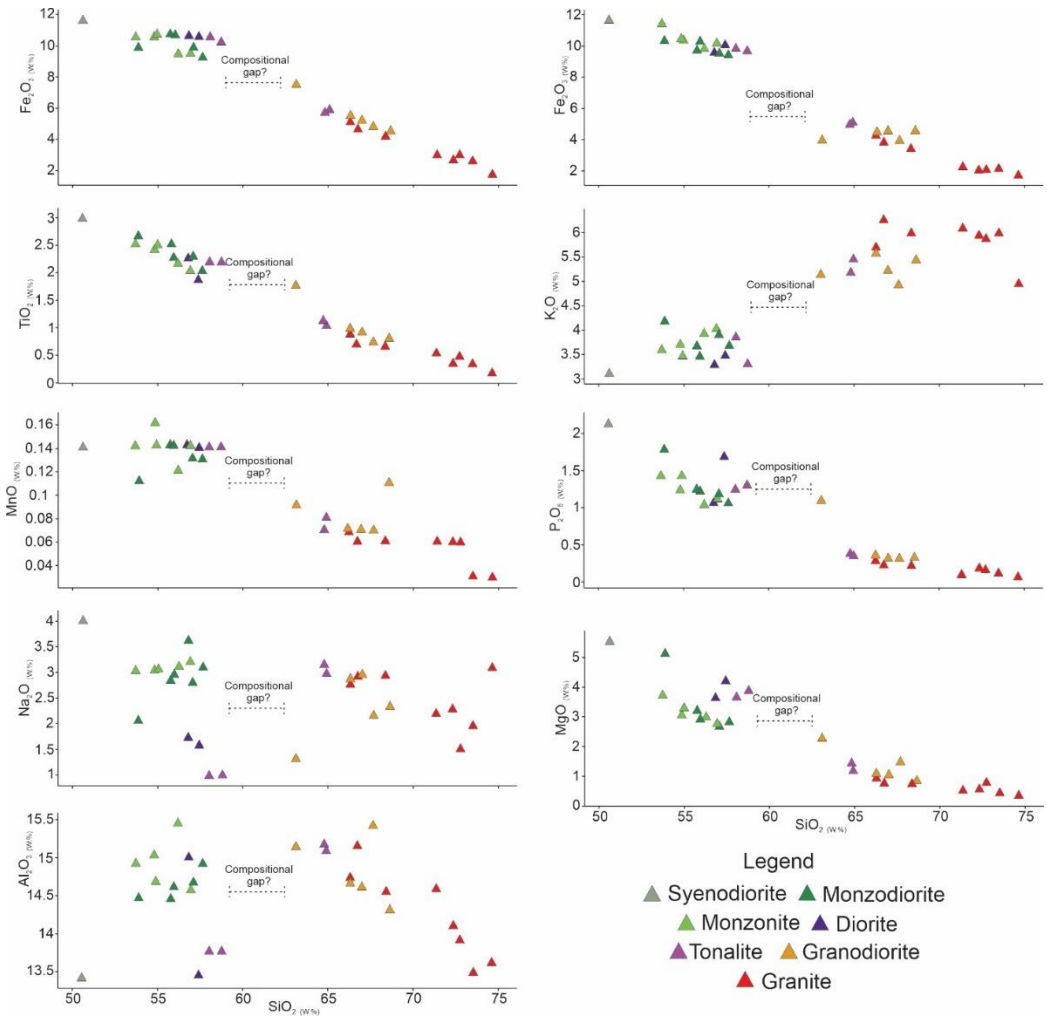


**Figure 7.** Harker diagrams for the CIC samples, showing two groups with distinct characteristics separated by a compositional gap.

Figure 8 presents the principal component analysis performed with the main oxides (Figure 8A) and the trace elements (Figure 8B) available in the compiled works. The possible compositional gap demonstrated in the Harker diagrams delimits two large sets of rocks in the CIC, and this same pattern is observed in the principal component analysis (Figure 8A). The group composed of granites, granodiorites, and two tonalite samples (group 1) is strongly influenced by the $SiO_2$ and $K_2O$ vectors, where the low angle between the vectors demonstrates their high correlation. The second group, composed of syenodiorite, monzodiorite, monzonite, diorite, and two tonalite samples (group 2), is strongly influenced by the vectors CaO, $TiO_2$, $Fe_2O_3$, MnO, $P_2O_5$, and MgO, where the CaO-$TiO_2$, $Fe_2O_3$-MnO and $P_2O_5$-MgO pairs are highly correlated.

Preprints.org (www.preprints.org) | NOT PEER-REVIEWED | Posted: 6 November 2024 doi:10.20944/preprints202411.0370.v1



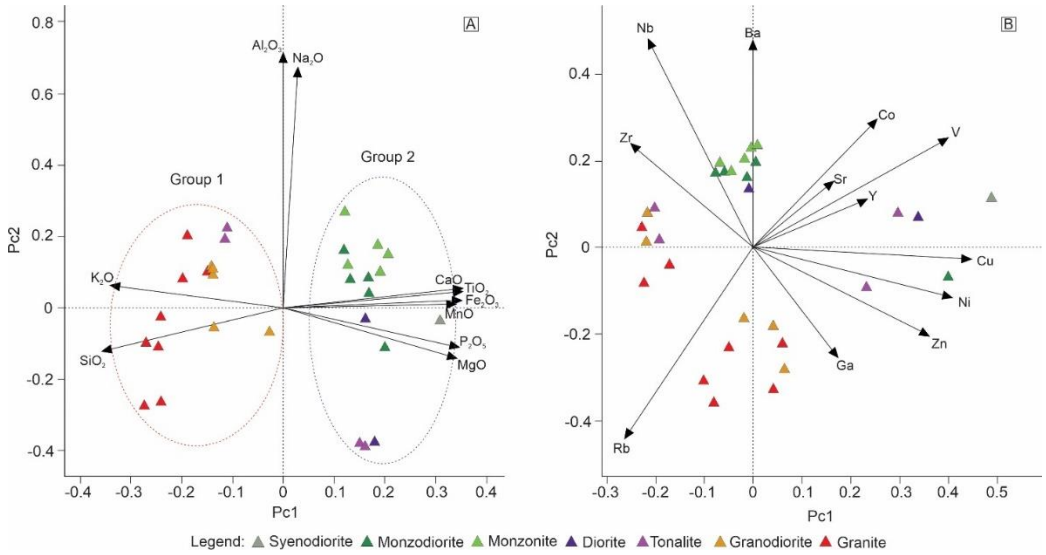


**Figure 8.** A) Principal component analysis for the major elements ($SiO_2$, $Al_2O_3$, $Fe_2O_3$, CaO, MgO, MnO, $Na_2O$, $K_2O$, $TiO_2$, $P_2O_5$) indicating two distinct groups for the CIC rocks. B) Principal component analysis for the trace elements indicating subdivision of group 1 and dispersed pattern of group 2.

The principal component analysis for the trace elements demonstrated that group 1 can be subdivided into two groups (Figure 8B). The behavior of Rb strongly influences one group, with some influence of Ga, and the other group is influenced by the behavior of Zr. Group 2 presents a more dispersed pattern (Figure 8B). However, a set of samples is strongly influenced by Ba and Nb.

Correlation matrices were calculated for the two large groups observed in the principal component analysis. Molar ratios were calculated for each oxide to standardize the elements, converted from % by weight to parts per million (ppm). In Figure 9, the color bar is associated with different $r^2$ values. The $r^2$ values are generally low to intermediate for both groups, except for the Fe-Si and Fe-Ti pairs in group 1, where the $r^2$ values are more significant than 0.8 (Figure 9).

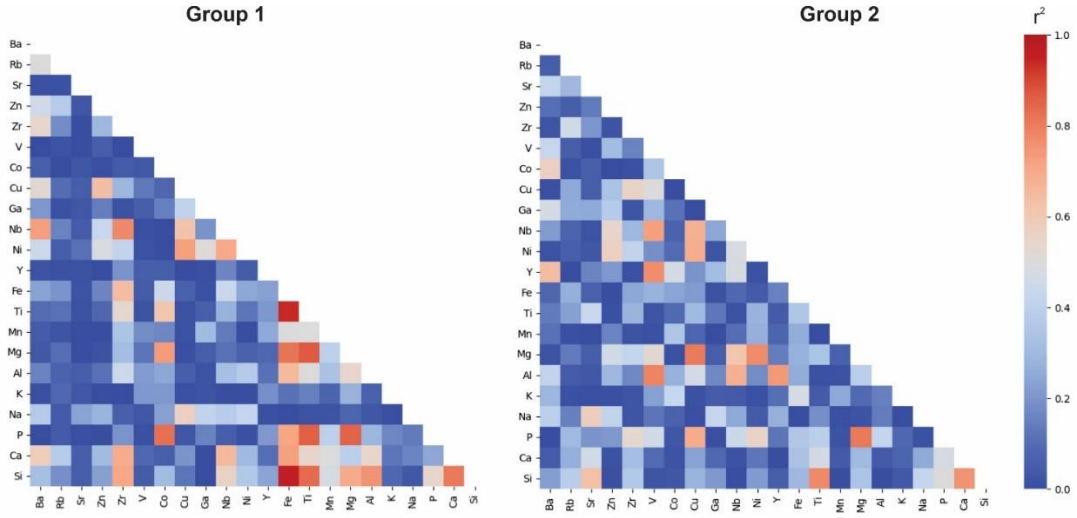


**Figure 9.** Correlation matrices for major and trace elements in the Castelo Intrusive Complex's geochemical groups 1 and 2. The color bar on the right indicates the colors associated with different $r^2$ values.

In the multielement diagram with samples normalized to the chondrite [64] (Figure 10), the set of rocks from group 1 shows a more significant negative anomaly in Eu than the samples from group 2. Both groups were observed to present pronounced ETRL enrichment to ETRP. In the multielement diagram with samples normalized to the primitive mantle [65] (Figure 10), the set of rocks from group

 doi:10.20944/preprints202411.0370.v1



2 presents negative anomalies for Ti, Zr, Sr, and Nb and enrichment for Ba, Th, U, La, and Nd. The set of rocks from group 1 presents a pattern with negative anomalies in Ti, P, Sr, and Nb, differing only for a strongly positive anomaly in Zr, in addition to Th and Nd.

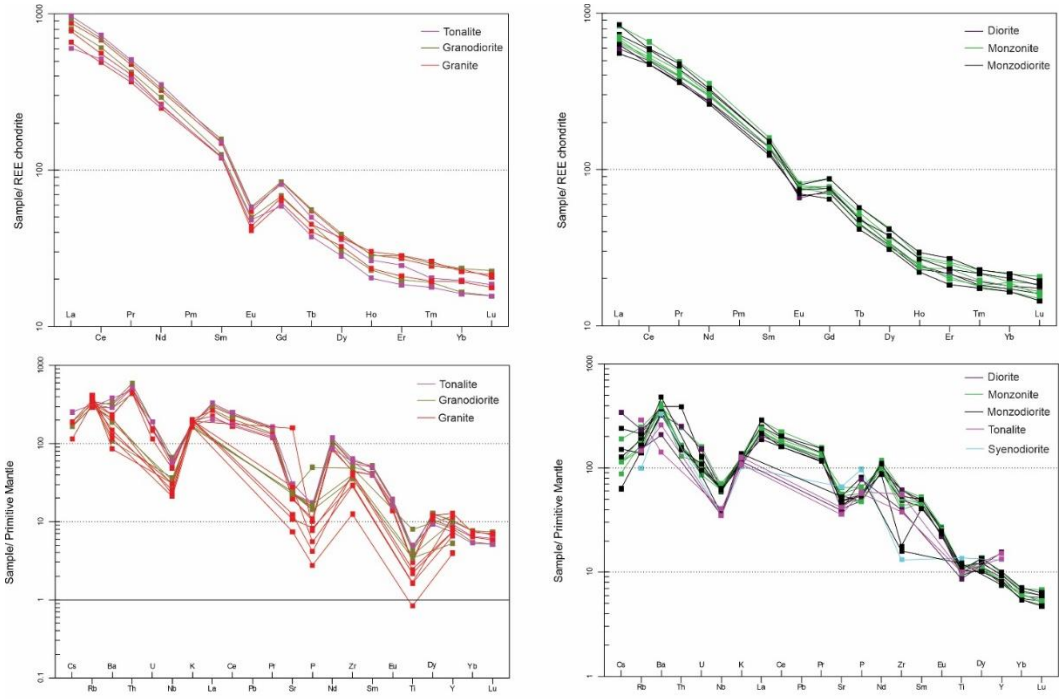


**Figure 10.** Multielement diagrams of the CIC normalized for the chondrite [64] and the primitive mantle [65].

The granitoids of the CIC can be classified as ferrous to weakly metaluminous, alkaline-calcic to calc-alkaline, with a positive trend between the silica content and the $Na_2O+K_2O-CaO$ parameter, and meta- to peraluminous saturated in silica, according to the diagrams of [66] (Figure 11). The classification proposed by [66] determines the rocks of group 2 as having originated in alkaline arc environments. (Figure 12).

Preprints.org (www.preprints.org) | NOT PEER-REVIEWED | Posted: 6 November 2024 doi:10.20944/preprints202411.0370.v1



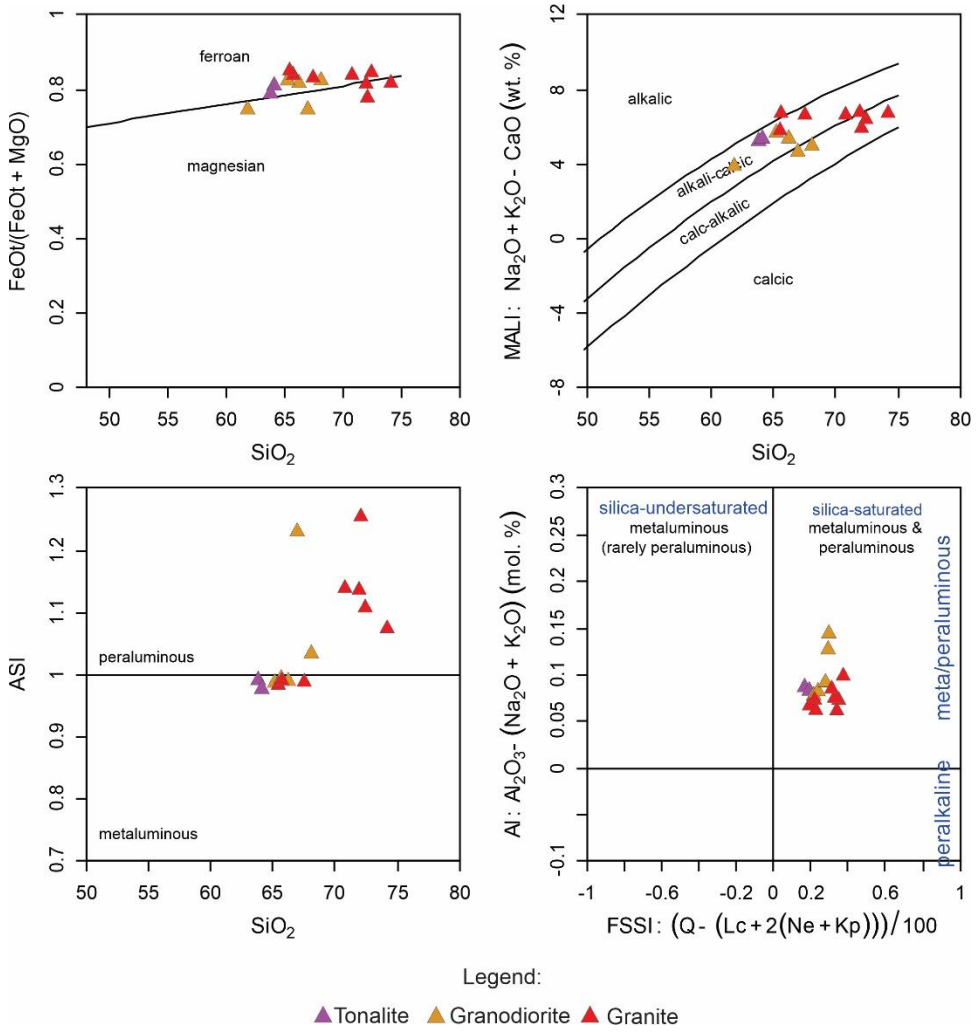


**Figure 11.** A) $FeO_t/(FeO_t + MgO)$ vs. $SiO_2$ diagram according to [66]. B) $SiO_2$ vs. $Na_2O+K_2O$-CaO diagram according to [66]. C) $SiO_2$ vs. ASI diagram, D) FSSI vs. AI diagram according to [66].

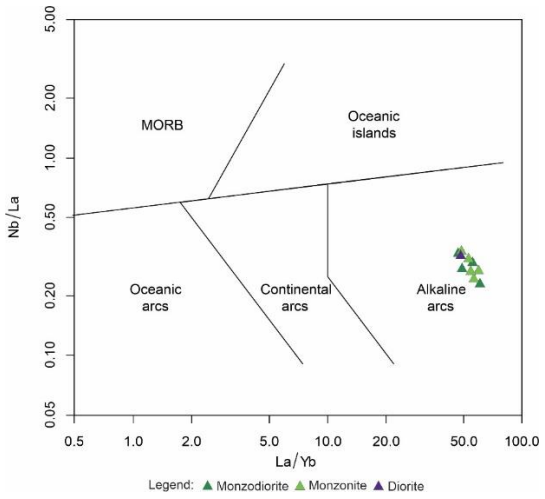


**Figure 12.** Tectonic discrimination diagram for the rocks of group 2 of the CIC, according to [66].

*5.3. U-Pb Results*

Three samples from the CIC were analyzed, two of which were related to granites from the northern and western edges of the massif, and the diorite located in the core. Analytical results are

 doi:10.20944/preprints202411.0370.v1



presented in supplementary material B. Sample FGIL 01, corresponding to the granite from the northern edge, presents euhedral zircon crystals, prismatic habits, compositional zonation, and homogeneous cores (Figure 13). The sample provided an upper intercept age of 504 ± 6 Ma and MSWD of 0.62 (Figure 14).

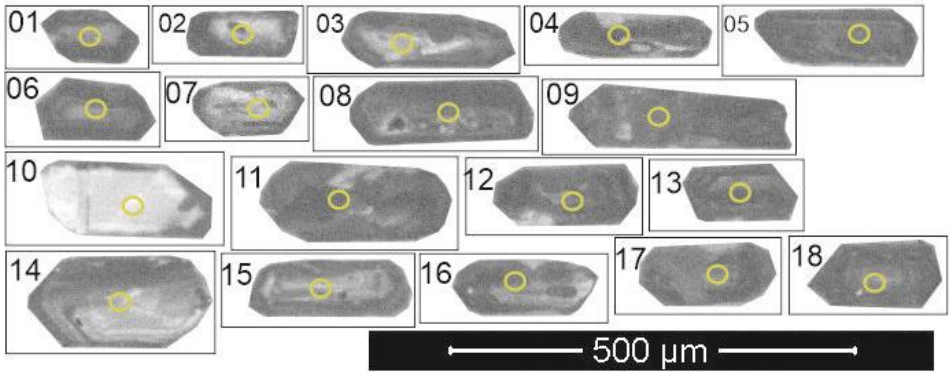


**Figure 13.** Cathodoluminescence images of sample FGIL 01. The yellow circles correspond to the U-Pb spots.

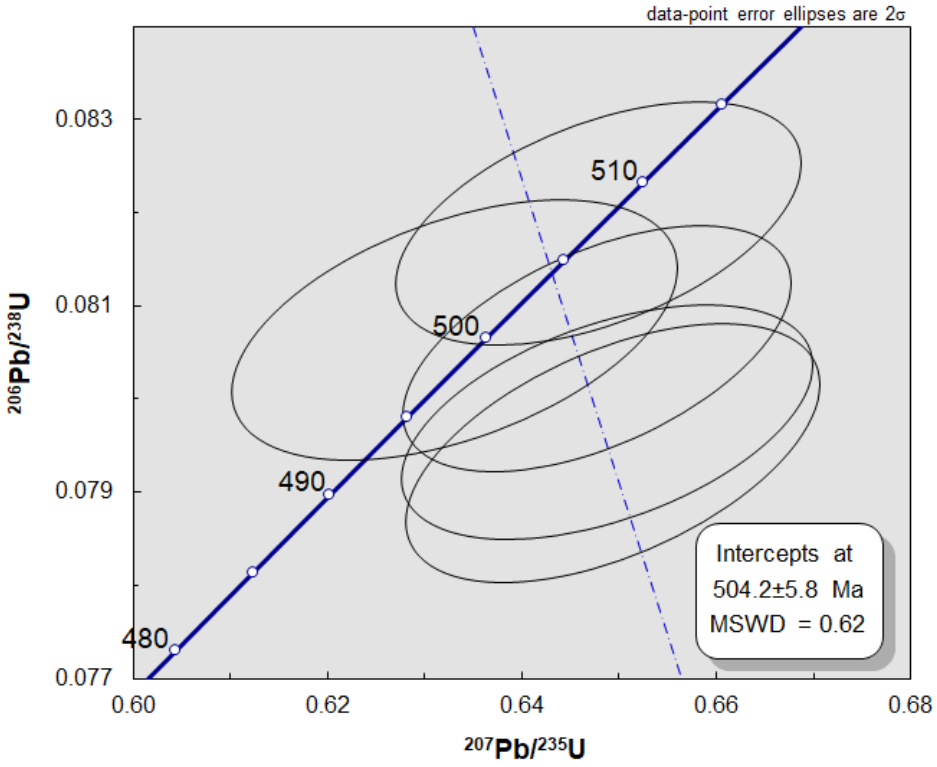


**Figure 14.** Concordia diagram for sample FGIL 01.

Sample FGIL 37 corresponds to the diorite from the massif's core. The zircon crystals are euhedral to subhedral and show prismatic to subrounded habits, compositional zonation, and homogeneous colors (Figure 15). The sample yielded a 514 ± 6 Ma crystallization age and MSWD of 0.032 (Figure 16).

Preprints.org (www.preprints.org) | NOT PEER-REVIEWED | Posted: 6 November 2024 doi:10.20944/preprints202411.0370.v1



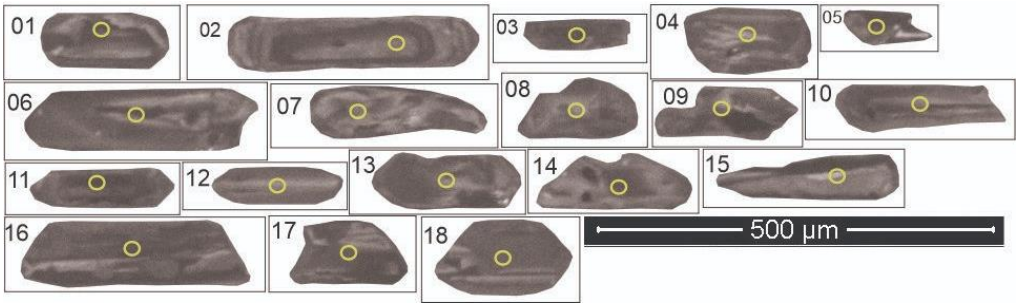


**Figure 15.** Cathodoluminescence images of sample FGIL 37. The yellow circles correspond to the U-Pb spots.

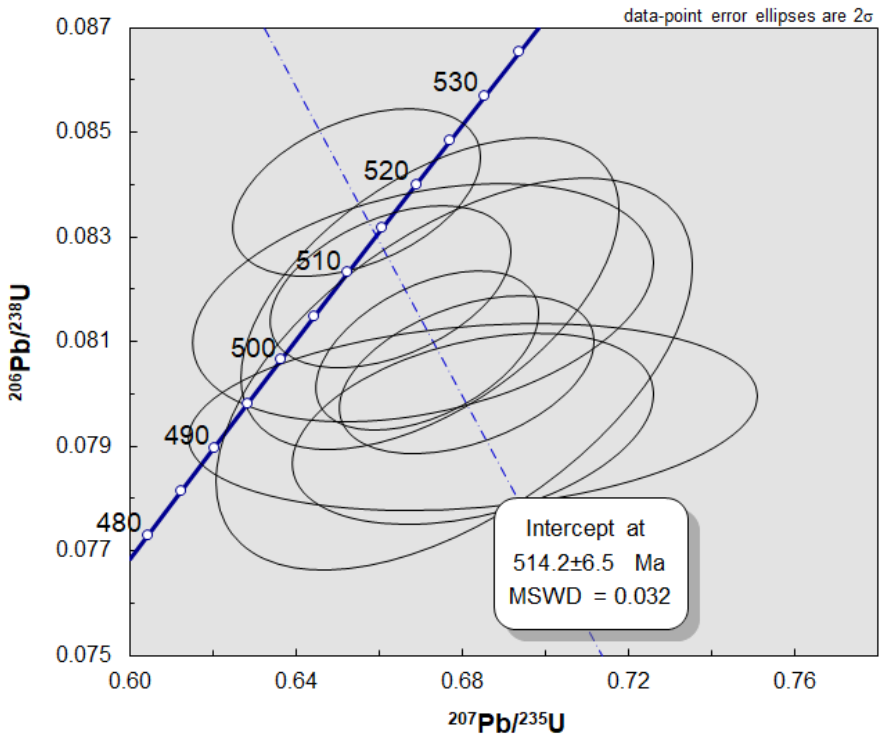


**Figure 16.** Concordia diagram for sample FGIL 37.

Sample FGIL 45 corresponds to the granite from the western edge of the CIC. The zircon crystals are euhedral and show prismatic habits, sometimes with bipyramidal terminations, compositional zonation, and homogeneous cores (Figure 17). This sample yielded a crystallization age of 529 ± 3 Ma and an MSWD of 2.7 (Figure 18).

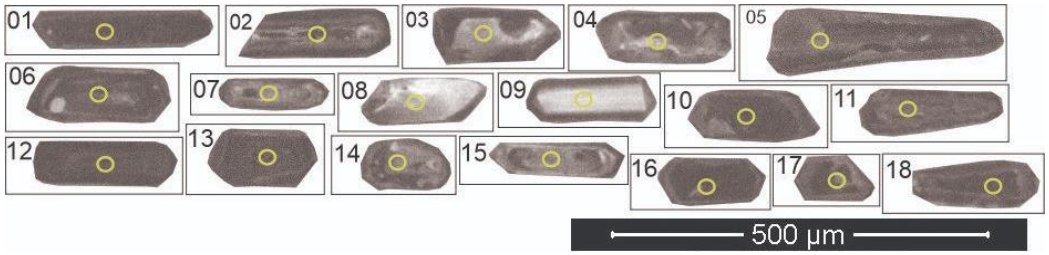


**Figure 17.** Cathodoluminescence images of sample FGIL 45. The yellow circles correspond to the U-Pb spots.

Preprints.org (www.preprints.org) | NOT PEER-REVIEWED | Posted: 6 November 2024 doi:10.20944/preprints202411.0370.v1



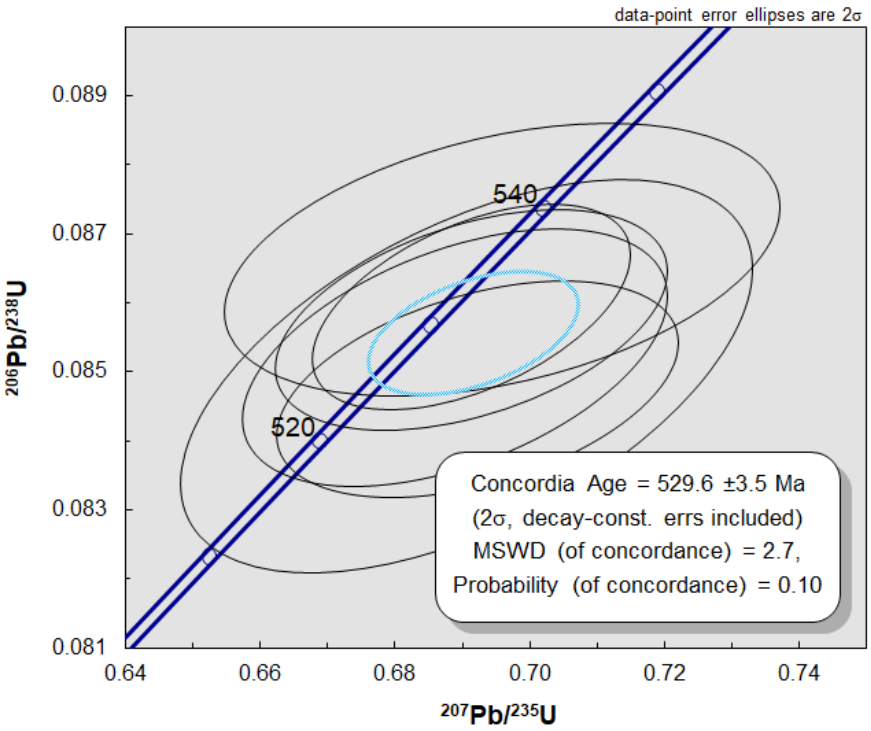


**Figure 18.** Concordia diagram for sample FGIL 45.

## 6. Discussions

### *6.1. Geological Units*

The Castelo Intrusive Complex (CIC) has been studied since the 1990s, and since then, several mapping works have been carried out in this intrusive complex, each with its specific focus. As a result, different geological maps have been presented in recent decades [14,37,38,40,42,68]. The map presented in this work results from extensive facies mapping work in the CIC, which has been developed to standardize the different maps presented so far. The diversity of rocks present in the CIC is evident in all works.

Monzogranite is the main unit in the CIC and is related to the highest altitudes and steep reliefs. It also presents two facies variations. The fine- to coarse-grained inequigranular monzogranite outcrops on the edge of the massif, in the western portion and south-central. Porphyritic monzogranite outcrops in the innermost portions and on the eastern edge of the CIC, with K-feldspar phenocrysts that reach 6 cm and indicate magmatic flow. Both have the same mineralogy and are cut by pegmatite veins and dikes, in addition to exhibiting xenoliths of the host rock and features related to magma mixing, such as micro granular mafic enclaves, features analogous to schlieren and agmatic structures (Figures 4 and 5).

Granodiorite and quartz-monzodiorite are predominant units in the south-central portion of the massif (Figures 4 and 5). However, quartz-monzodiorite is present in a restricted form in other portions of the CIC. They are mesocratic to melanocratic rocks, fine-grained, frequently cut by coarse-grained granite injections. The granodiorite presents a salt-and-pepper texture and microgranular mafic enclaves, small plagioclase xenocrysts, mostly rounded, and clots of mafic minerals of a few centimeters. The quartz-monzodiorite is the unit that presents the most features related to magma mixing, such as chilled margins, features analogous to pillows, rounded, corroded feldspar xenocrysts, inclusion zones of mafic minerals in the xenocrysts, mixing zones, compositional zoning, plagioclase laths with evidence of corrosion on the edges, boxy cellular textures, synesis, zones of mafic minerals, crystalline inversion, a mix of apatite crystals and poikilitic texture.

Diorite is the unit that outcrops in the core of the massif in a region of low topography surrounded by granite scarps. It is melanocratic, equigranular, medium to coarse-grained, presents

 doi:10.20944/preprints202411.0370.v1



mafic clots of a few centimeters, and is frequently cut by coarse-grained granite injections. Aggregates of biotite and hornblende are common, as are quartz xenocrysts, which show the ocellar quartz-hornblende texture when surrounded by hornblende crystals (Figures 4 and 5).

*6.2. The Mixing Process: Field and Petrographic Evidences*

Associated with the diversity of rocks, field features show an important process: the physical dispersion of contrasting magmas – magma mixing. This same process is observed in other intrusive complexes of the G5 super suite as well as in other plutons in Brazil and the world, for example [14,70–73]. The main field evidence observed in the CIC that points to a process of magma mixing is the mafic microgranular enclaves, recurrent in the monzogranites, pillow-like dikes, net-veined, and migration of feldspar megacrysts. According to [74], a single texture cannot be used as evidence of magma mixing but rather a set of them in the CIC.

Microgranular mafic enclaves in the host monzogranite are recurrent in the CIC. Many authors consider that microgranular mafic enclaves would be the result of the mixing of felsic and mafic magmas [75–77]. However, they can be interpreted as "bubbles" or "globules" that were produced in the mantle and mixed with felsic rocks of crustal origin [78–80]. Other authors, however, consider the enclaves as remnants of the partial melting of the rock that gave rise to the granitoids; therefore, the enclaves would be residues of the most refractory minerals [81–83]. In the case of the CIC, some textures in the mafic enclaves point to an interaction between two contrasting magmas. The rounded shapes indicate the disintegration of the mafic magma with the felsic magma [80]. The fine grain of the enclaves probably consists of rapid crystallization due to thermal equilibrium between a high-temperature magma and a low-temperature magma [80,84].

The cooled margins and syn-plutonic dikes suggest temperature differences between the magmas that mix [85]. K-feldspar phenocrysts occur in enclaves as xenocrysts. This happens when phenocrysts from the host rock can overcome the edges of microgranular mafic enclaves and crystallize within them [76,77,86]. The mechanisms for a phenocryst to become a xenocryst involve mechanical migration or capture processes [87], where partial dissolution of K-feldspar crystals is common, making them rounded [88].

Crenulated, lobed, and cusp contacts reinforce the existence of different magmas coexisting, which had low viscosity and/or high resistance to flow when they came into contact [77,80,85]. According to [78], net-veined structures form in the portions of the magma chamber where mafic magma is abundant. Examples of net-veined structures were described by [89] in the British Igneous Province. Physical dispersion between contrasting magmas can form pillow-like features, representing portions of the host mafic rock individualized by the intrusion and with a rounded shape. A type similar to those described is the agmatic analogous features, distinguished by the lack of pattern in their shapes and their chaotic appearance. Both features are recognized in the Santa Angélica Intrusive Complex [37,43].

Petrographic evidence such as zoned crystals, box cellular and synnesius textures in plagioclase, corroded and rounded crystals, ocellar quartz, mafic mineral clots, acicular apatite and poikilitic crystals are indicative of mixing between mafic and felsic magmas. Zonation is indicative of sudden variations in crystallization conditions, such as composition and nucleation, and growth rates of crystals, representing an excellent record of thermodynamic variations during magma mixing [90–92]. The boxy cellular texture in plagioclases can be interpreted as the result of a high growth rate and low nucleation rate. The cooling of the environment caused by heat transfer from the heat to the cooler magma during mixing may be ideal for forming the texture [90].

Plagioclase with poikilitic texture is also formed by thermal disequilibrium with the matrix of fine-grained mafic rocks. Plagioclase crystals present inclusions of minerals such as quartz, hornblende, biotite, and opaques [90]. Fine graining and plagioclase laths are common in hybrid rocks, which form due to relatively rapid crystallization, favoring a high nucleation rate [90,93]. The formation of the synneusis texture occurs by the joining of plagioclase crystals suspended in the magma. Quartz mantled by ocellar hornblende consists of a coarse-grained and rounded quartz xenocryst with inclusions of tiny hornblende crystals on its rim. [75] and [90] highlight the mixture

 doi:10.20944/preprints202411.0370.v1



of two systems, one more felsic with early quartz crystals and the other more mafic systems containing tiny hornblende crystals. Acicular apatite crystals are formed due to the rapid cooling (quenching) of mafic magma incorporated into a felsic host rock, which already has prismatic apatite crystals [90,94]. Mafic clots comprise hornblende, biotite, opaques, titanite, and apatite crystals.

### *6.3. The Source Evidences*

The lithological variety of the CIC is also expressed in the lithogeochemical data set, especially in the wide range of $SiO_2$ contents (50.19% to 74.14%) and in the variation observed in the R1-R2 diagram for the classification of plutonic rocks, where the rocks were classified as syenodiorite, monzodiorite, monzonite, diorite, tonalite, granodiorite, and granite. The silica variation observed in the Harker diagrams demonstrated a "compositional gap," which reinforces the interaction of magmas from different sources that interacted with each other [9,77,90,92].

The principal component analysis (Figure 8) reinforces the existence of two large groups of rocks, group 1 being composed of granites, granodiorites, and tonalites, and group 2 being composed of granodiorites, mozo diorites, monzonites, diorites, and tonalites. The principal component analysis performed with trace elements demonstrated the existence of 2 subgroups among the rocks of group 1, one being strongly controlled by the concentrations of Rb and the other controlled by the concentrations of Zr. In group 2, a diorite, monzonite, and monzodiorite subgroup presents low dispersion, and the other samples present a dispersed pattern in the diagram.

The correlation matrices between the principal components reveal the prominent role of the magma mixing process. The low values observed in general (colors in shades of blue) show a strong correlation between the elements and the effectiveness of the mixing process. The strong correlation between the elements is facilitated in the mixing process by the diffusion process of the chemical elements present in the different magmas. Chemical exchanges are suggested by the advection process, where the contact area between the interacting magmas increases exponentially as a function of time. Consequently, chemical diffusion becomes progressively more efficient [77,95–98].

The normalized multi-element diagram to chondrite [64] shows similarities between the two groups of rocks of the CIC. Among them, the negative Eu anomaly was more pronounced for group 1 and enrichment in ETRL, with pronounced fractionation. The multielement diagram normalized to the primitive mantle [65] shows some similarities for the two sets of rocks, with very similar values in the content of Ti, Nb, Sr, K, Ba, Th, and U. This demonstrates geochemical affinity between the different types of rock, and the crustal contamination in the most mafic members is attested by the enrichment of elements such as K, Ba, Rb, Sr and the ETRL.

Finally, the classification diagrams demonstrate that the rocks of the CIC are ferrous to weakly metaluminous, alkaline-calcic to calc-alkaline, with a positive trend between the silica content and the $Na_2O+K_2O$-CaO parameter, and meta- to peraluminous saturated in silica, according to the diagrams of [66], and originated in alkaline arc environments.

In addition to the magma mixing process, which presents much evidence, the assimilation process is also a factor to be considered for the rocks of the CIC. Many xenoliths of the host rock are observed in the massif. The main host rock of the CIC is orthogneiss, followed by biotite-garnet gneiss with migmatization features and marble. The host orthogneiss of the CIC was defined by [24] as the Caxixe Batholith, constituting rocks of granodioritic to granitic composition, with tonalites and gabbros present, calc-alkaline, metaluminous to weakly peraluminous, enrichment in ETRL and patterns similar to the rocks of the CIC in the multielement diagrams normalized to the primitive mantle. In addition, they present positive and negative values of $\varepsilon Hf(t)$ and $\varepsilon Nd$.

### *6.4. U-Pb and Lu-Hf Signatures*

The U-Pb and Lu-Hf analyses for the rocks of the CIC are presented here, and the data reported by [15] are used here to constrain the emplacement timing of the study rocks. Three samples of monzogranite, one sample of quartz-diorite, and one sample of hololeucocratic dike. The U-Pb zircon ages yielded five new ages for the CIC, showing a peak of magma production around 500 ± 15 Ma,

 doi:10.20944/preprints202411.0370.v1



ranging from 527 ± 3 Ma to 427 ± 5 Ma. Three analyses were performed on zircon grains from the monzogranitic component, one on a quartz-diorite sample and one on a hololeucocratic dike sample.

The analyzed samples show positive and negative values of $\varepsilon Hf_{(t)}$, with maximum values between +12.70 and -39.5. The model ages (TDM) presented range from the Paleoproterozoic to the Neoproterozoic, showing a pattern of Paleoproterozoic ages for negative $\varepsilon Hf_{(t)}$ values. In contrast, the Neoproterozoic ages are related to positive $\varepsilon Hf_{(t)}$ values. Another characteristic of the samples analyzed is that they all indicate mantle and crustal sources.

**Table 2.** Summary of U-Pb geochronological and Lu-Hf isotopic data from the CIC compiled from [68] and [69].

| SAMPLE | ROCK | U-Pb AGE | MSWD | $^{176}Hf/^{177}Hf$ | $\varepsilon_{Hf}$ (t) | $T_{DM}$ AGES (Ga) |
|---|---|---|---|---|---|---|
| FGIL 06 A | Monzogranite | 499 ± 4 | 1.12 | 0.28142 to 0.28268 | +10.7 and -13.2 | 0.75 to 2.11 |
| FGIL 11 A | Monzogranite | 524 ± 5 | 1.4 | 0.28134 to 0.28275 | + 12.6 and – 22.0 | 0.64 to 2.60 |
| FGIL 17 A | Monzogranite | 521 ± 14 | 0.49 | 0.28142 to 0.28300 | +11.3 and -24.0 | 0.72 to 2.71 |
| FGIL 06 B | Qtz-Monzodiorite | 486 ± 12 | 0.43 | 0.28181 to 0.28281 | +12.57 and -22.7 | 0.65 to 2.64 |
| FGIL 06 C | Hololeucocratic dyke | 432 ± 32 | 1.17 | 0.28155 to 0.28281 | +12.7 and -24.0 | 0.64 to 2.71 |

The new U-Pb data in zircon confirm that the peak of magma production in the CIC corresponds to the post-collisional stage of the Araçuaí Orogeny, between 530 and 480 Ma [36,38,45,47–50]. Isotopic studies of $^{87}Sr/^{86}Sr$ and $^{143}Nd/^{144}Nd$ presented by [38] and references therein suggested that the gabbroic rocks of the G5 supersuite are the product of partial melting of a previously enriched mantle during the onset of subduction in the Araçuaí Orogeny. A previously enriched mantle may be one of the sources for the generation of basaltic magmas, which is partially corroborated by the low $^{176}Hf/^{177}Hf$ ratios obtained by [15] for the quartz-monzodiorite of the CIC. However, [15] also obtained zircon grains with high $^{176}Hf/^{177}Hf$ ratios and positive $\varepsilon Hf_{(t)}$ values for this same quartz-monzodiorite from the CIC, which demonstrates that a depleted mantle component is also present. Here, an important discussion arises regarding the mantle source of the G5 supersuite: does only one mantle reservoir act as a source, or, as with magmatism associated with mantle plumes, is more than one mantle reservoir present?

The significant variation between the $\varepsilon Hf_{(t)}$ values, which reach around 30 units, can be explained by the interaction process of magma originating from the crust and the mantle. This variation is observed within each sample analyzed, corroborating that the zircons in these rocks have distinct isotopic compositions and were subsequently agglutinated in the same volume of rock, preserving this considerable isotopic variation [100,101]. Some plutons of the Araçuaí Orogeny also exhibit positive and negative values of $\varepsilon Hf_{(t)}$, as is the case of the Afonso Cláudio, Barra de São Francisco and Santa Angélica Intrusive Complexes [34,45,50] corroborating the fact that different sources of magmas were present in the formation of these massifs, and which are also confirmed by field, petrographic and lithogeochemical evidence, unlike that suggested for the Várzea Alegre and Venda Nova Intrusive Complexes [103], which do not take into account the evidence of magma mixing, including that suggested by other authors for the same massifs [38,45,48,49].

The TDM ages range from 2.7 Ga to 1.41, and together with the $\varepsilon Hf_{(t)}$ values, they corroborate with different magma sources for the CIC, one mantle source, and at least two crustal sources. The negative $\varepsilon Hf_{(t)}$ values observed in all samples show Neoproterozoic TDM ages, ranging from 0.64 Ma to 1.18 Ma, thus constituting an important juvenile reservoir. The $\varepsilon Hf_{(t)}$ values between -26 and -22 show Archean to Paleoproterozoic TDM ages (2.6 to 2.4 Ga), while the samples with $\varepsilon Hf_{(t)}$ values between -17 to -8 are essentially Paleoproterozoic (2.2 Ga to 1.7 Ga).

[46] and [50] discuss the possibility of different crustal sources for the Pedra Azul and Santa Angélica Intrusive Complexes, respectively. As observed in the CIC, an older crustal source appears in both. Therefore, some candidates appear as possible older crustal sources [16] report Archean and

 doi:10.20944/preprints202411.0370.v1



Paleoproterozoic TDM ages, in addition to positive and negative values of $\varepsilon Hf_{(t)}$ for rocks of the Caparaó Complex, showing similarities with the signatures observed in the CIC. Other possible candidates that are presented are the Juiz de Fora and Pocrane Complexes, basements of the Araçuaí Orogeny [21,51,104]. The rocks of the Juiz de Fora and Pocrane Complex, which represent the basement of the Araçuaí Orogeny, also present positive and negative values for $\varepsilon Hf_{(t)}$ and $\varepsilon Nd_{(t)}$, in addition to TDM ages in the Archean to Paleoproterozoic transition.

An important Paleoproterozoic candidate for the crustal source of the CIC is the granitoids of the G1 supersuite [39]. Hf and Nd data for rocks of the Estrela Orthogneiss in the Castelo region indicate values ranging from -9.2 to -4.7 and Paleo to Mesoproterozoic TDM ages ranging from 2.2 to 1.4 Ga [105]. The host of the CIC, the Caxixe batholith [24], presents U-Pb ages in zircon around 850 Ma, correlated with the Serra da Prata magmatic arc of the Ribeira Orogeny [32]. These rocks present positive $\varepsilon Hf_{(t)}$ values, between +10 and +14, and a Neoproteorozoic model age. [33] also present for the Caxixe batholith, rocks compatible with the G1 supersuite of the Araçuaí Orogeny, between 630 and 580 Ma, with negative Hf values, between -4 and -13, and TDM ages between 1.33 and 1.67.

## 7. Conclusions

The Castelo Intrusive Complex (CIC) reveals a complex interaction between magmas of different compositions and sources, evidenced by both petrographic and structural features and lithogeochemical and isotopic data. Mixing magmas is widely supported by microgranular mafic enclaves, specific textures such as ocellar quartz and K-feldspar phenocrysts, and field features such as syn-plutonic dikes and pillow-type volcanic rocks.

In addition to the mixing of magmas, the isotopic data suggests the participation of multiple mantle and crustal sources in the genesis of the CIC, with significant variations in the values of $\varepsilon Hf_{(t)}$ and TDM model ages. These data corroborate the hypothesis of contribution from enriched and depleted mantle reservoirs and multiple crustal sources. These data indicate a complex interaction of post-collisional magmatic processes in the context of the Araçuaí Orogeny, reinforcing the importance of investigating multiple reservoirs to understand the tectonic-magmatic evolution of this Orogeny.

This mechanism may have been facilitated by the delamination of the very thick lithosphere with significant elevations with high gravitational potential and the enrichment of the mantle through the slab at the end of the collisional stage. These elements lead to lateral flow that facilitated the intrusion of basic magmas formed by the partial melting of an asthenospheric mantle and crustal magmas generated by the heat provided by the rising mantle. In this sense, the process of decompression of the lower crust provided sufficient heat for crustal anatexis, where later magmatic mechanisms of physical dispersion (mingling) and chemical diffusion (mixing) favored hybridization. However, it is considered that this was not a process that occurred all at once; the subtle differences in the chemical and isotopic signatures shown in the rocks of the ICC lead to the belief that several pulses and different portions of the crust were responsible for the formation of the magmas that originated the ICC.

**Author Contributions:** Conceptualization: Iago Mateus Lopes de Macêdo, Guilherme Loriato Potratz, Marilane Gonzaga Melo, Mauro Cesar Geraldes, Rodson Marques de Abreu; Methodology: Iago Mateus Lopes de Macêdo, Guilherme Loriato Potratz, Marilane Gonzaga Melo, Mauro Cesar Geraldes, Rodson Marques de Abreu; formal analysis: Iago Mateus Lopes de Macêdo, Guilherme Loriato Potratz, Mauro Cesar Geraldes, Renzo Dias Rodrigues, Ana Paula Meyer, Armando Dias Tavares, Marco Machado da Silva; investigation: Iago Mateus Lopes de Macêdo, Marilane Gonzaga Melo, Mauro Cesar Geraldes, Rodson Marques de Abreu; resources: Mauro Cesar Geraldes, Aramando Dias Tavares; writing—review and editing: Iago Mateus Lopes de Macedo, Guilherme Loriato Potratz, Mauro Cesar Geraldes; visualization: Iago Mateus Lopes de Macedo, Guilherme Loriato Potratz, Mauro Cesar Geraldes. All authors have read and agreed to the published version of the manuscript.

**Acknowledgments:** The authors thank the funding agencies. Guilherme Loriato Potratz thanks Fundação Carlos Chagas Filho de Amparo à Pesquisa do Estado do Rio de Janeiro for his postdoctoral scholarship, process numbers E26-204.530/2021 and E26-204.531/2021. Mauro Cesar Geraldes thanks the National Council for Scientific and Technological Development (CNPq) for the research grant (process nº 301470/2016-2).

 doi:10.20944/preprints202411.0370.v1



**Conflicts of Interest:** The authors declare no conflict of interest.

## References


1. Song, S.G., Wang, M.J., Wang, C., Niu, Y.L., 2015. Magmatism during a continental collision, subduction, exhumation and mountain collapse in collisional Orogenic belts and continental net growth: A perspective. Sci. China-Earth Sci. 58, 1284–1304.
2. Bonin, B. 2004. Do coeval mafic and felsic magmas in post-collisional to within-plate regimes necessarily. Imply two contrasting, mantle and crustal, sources? A review. Lithos v.78, p.1 – 24.
3. Liégeois, J.P. 1998. Some words on the post-collisional magmatism – Preface to Special Edition on Post-collisional Magmatism. Lithos, 45: xv-xvii
4. Sklyarov, E.V., Federovskii, V.S. 2006. Magma Mingling: Tectonic and Geodynamic Implications. Geotectonics, Vol. 40, No. 2, pp. 120–134
5. Perugini, D., Petrelli, M., Poli, G., De Campos, C., Dingwell, D.B., 2010. Recent phlegrean field eruptions' time-scales are inferred from applying a "diffusive fractionation" model of trace elements. Bulletin of Volcanology 72, 431–447.
6. Sami, M., Ntaflos, T., Farahat, E.S., Mohamed, H.A., Hauzenberger, C., Ahmed, A.F., 2018. Petrogenesis and geodynamic implications of Ediacaran highly fractionated A type granitoids in the north Arabian-Nubian Shield (Egypt): constraints from whole rock geochemistry and Sr-Nd isotopes. Lithos 304 (307), 329–346. https://doi.org/10.1016/j.lithos.2018.02.015.
7. Wang, Q., Zhao, J., Zhang, C., Yu, S., Ye, X., Liu, X. 2022. Paleozoic post-collisional magmatism and high-temperature granulite-facies metamorphism coupling with lithospheric delamination of the East Kunlun Orogenic Belt, NW China. Geoscience Frontiers 13, 101271. https://doi.org/10.1016/j.gsf.2021.101271
8. Perugini, D., De Campos, C.P., Dingwell, D.B., Dorfman, A., 2013. Relaxation of concentration variance: a new tool to measure chemical element mobility during mixing of magmas. Chemical Geology 335, 8–23.
9. De Campos, C.P. 2015. Chaotic flow patterns from a deep plutonic environment: A case study on natural magma mixing. Pure Applied Geophysics. 172, 1815–1833. https://link.springer.com/article/10.1007/s00024-014-0940-6.
10. Gagnevin, D., Daly, J.S., Kronz, A., 2010. Zircon texture and chemical composition as a guide to magmatic processes and mixing in a granitic environment and coeval volcanic system. Contribuitions Mineral Petrology, 159:579–596.
11. Yang, J.H., Wu, F.Y., Wilde, S.A., Xie, L.W., Yang, Y.H., Liu, X.M. 2007. Tracing magma mixing in granite genesis: in situ U–Pb dating and Hf-isotope analysis of zircons. Contribuitions Mineral Petrology, 153:177–190.
12. Pedrosa-Soares, A.C., Campos, C.P.C., Noce, C., Silva, L.C., Novo, T., Roncato, J., Medeiros, S., Castaneda, C., Queiroga, G., Dantas, E., Dussin, I., Alkmim, F., 2011. Late Neoproterozoic-Cambrian granitic magmatism in the Aracuai Orogeny (Brazil), the Eastern Brazilian Pegmatite Province and related mineral resources. In: Sial, A.N., Bettencourt, J.S., De Campos, C.P., Ferreira, V.P. (Eds.), Granite-Related Ore Deposits. Geological Society, Special Publications, London, pp. 25–51
13. Pedrosa-Soares, A.C., Deluca, C., Araujo, C., Gradim, C., Lana, C., Dussin, I., Silva, L.C., Babinski, M., 2020. O Orógeno Araçuaí à luz da geocronologia: um tributo a Umberto Cordani. In: Bartorelli, A., Teixeira, W., Brito Neves, B.B. (Eds.), Geocronologia e Evolução Tectônica do Continente Sul-Americano: a contribuição de Umberto Giuseppe Cordani. Solarias Edições Culturais, São Paulo, p. 728p.
14. De Campos, C.P., Medeiros, S.R., Mendes, J.C., Pedrosa-Soares, A.C., Dussin, I., Ludka, I.P., Dantas, E.L., 2016. Cambro-Ordovician magmatism in the Aracuai Belt (SE Brazil): Snapshots from a post-collisional event. Journal of South American Earth Science. 68, 248–268.
15. Macedo, I.M.L., Geraldes, M.C.G., Marques, R.A., Melo, M.G., Tavares, A.D., Martins, M.V.A., Oliveira, H.C., Rodrigues, R.D. 2022. New clues for magma-mixing processes using petrological and geochronological evidence from the Castelo Intrusive Complex, Araçuaí Orogeny (SE Brazil). Journal of South American Earth Sciences. 115, 103758. https://doi.org/10.1016/j.jsames.2022.103758.
16. Alkmin, F.F, Marshak, S, Pedrosa-Soares, A., Peres, G., Cruz, S.C.P, Whittington, A. 2006. Kinematic evolution of the Araçuaí–West Congo Orogeny in Brazil and Africa: Nutcracker tectonics during the Neoproterozoic assembly of Gondwana. Precambrian Research, 149:43 – 63.
17. Alkmin, F. F, Kuchenbecker, M, Reis, H. L. S, Pedrosa-Soares, A. C, 2017. The Araçuaí belt.In: Heilbron, M., Cordani, U.G, Alkmim F.F. (Eds.), São Francisco Craton, Eastern Brazil. Regional Geology Reviews, Springer International Publishing Co., pp. 255–276.
18. Tedeschi, M., Novo, T., Pedrosa-Soares, A.C., Dussin, I., Tassinari, T., Silva, L.C., Goncalves, L., Alkmim, F.F., Lana, C., Figueiredo, C., Dantas, E., Medeiros, S., De Campos, C., Corrales, F., Heilbron, M., 2016. The Ediacaran Rio Doce magmatic arc revisited (Aracuai- Ribeira Orogenyic system, SE Brazil). Journal of South American Earth Sciences. 68, 167–186.

 doi:10.20944/preprints202411.0370.v1




19. Almeida, F.F.M., Brito Neves, B.B., Carneiro, C.D.R. 2000. The origin and evolution of the South American Plataform. Earth Science Reviews., 50:77-111.
20. Heilbron, M.L., Pedrosa-Soares, A.C., Campos Neto, M.C., Silva, L.C., Trouw, R., Janasi, V.A., 2004. Brasiliano Orogenys in Southeast and South Brazil. Journal Virtual Explorer 17, Paper 4.
21. Degler, R., Pedrosa-Soares, A., Novo, T., Tedeschi, M., Silva, L.C., Dussin, I., Lana, C., 2018. Rhyacian-Orosirian isotopic records from the basement of the Aracuai-Ribeira Orogenyic system (SE Brazil): Links in the Congo-Sao Francisco palaeocontinent. Precambrian Research. https://doi.org/10.1016/j.precamres.2018.08.018
22. Corrales F.F.P., Dussin I.A., Heilbron M., Bruno H., Bersan S.A., Valeriano C.M., Pedrosa- Soares A.C., Tedeschi M. 2020. Coeval high Ba-Sr arc-related and OIB Neoproterozoic rocks linking pre-collisional magmatism of the Ribeira and Aracuai Orogenic belts, SE-Brazil, Precambrian Research. https://doi.org/10.1016/j.precamres.2019.105476.
23. Heilbron, M., Valeriano, C.M., Peixoto, C., Tupinambá, M., Neubauer, F., Dussin, I., Corrales, F., Bruno, H., Lobato, M., Almeida, J.C.A., Silva, L.G.E., 2020. Neoproterozoic magmatic arc systems of the central Ribeira belt, SE-Brazil, in the context of the West-Gondwana pre-collisional history: a review. Journal of South American Earth Sciences. 103, 102710 https://doi.org/10.1016/j.jsames.2020.102710.
24. Santiago, R., Caxito, F. A., Pedrosa-Soares, A., Neves, M.A., Calegari, S.S., Lana, C. 2022. Detrital zircon U–Pb and Lu–Hf constraints on the age, provenance and tectonic setting of arc-related high-grade units of the Araçuaí and Ribeira Orogenys (SE Brazil) transition zone. Journal of South American Earth Sciences, 116, 103861. https://doi.org/10.1016/j.jsames.2022.103861
25. Gradim, C., Roncato, J., Pedrosa-Soares, A.C., Cordani, U., Dussin, I., Alkmim, F.F., Queiroga, G., Jacobsohn, T., Silva, L.C., Babinski, M., 2014. The hot back-arc zone of the Aracuai Orogeny, Eastern Brazil: From sedimentation to granite generation. Brazilian Journal of Geology. 44, 155–180.
26. Gonçalves, L., Farina, F., Lana, C., Pedrosa-Soares, A.C., Alkmim, F., Nalini Jr., H.A., 2014. New U-Pb ages and lithochemical attributes of the Ediacaran Rio Doce magmatic arc, Araçuaí confined Orogeny, southeastern Brazil Journal of South American Earth Sciences. 52, 129–148. https://doi.org/10.1016/j.jsames.2014.02.008.
27. Gonçalves, L., Alkmim, F.F., Pedrosa-Soares, A.C., Dussin, I.A., Valeriano, C.M., Lana, C., Tedeschi, M., 2016. Granites of the intracontinental termination of a magmatic arc: an example from the Ediacaran Araçuaí Orogeny, southeastern Brazil. Gondwana Research. 36, 439–458. https://doi.org/10.1016/j.gr.2015.07.015.
28. Gonçalves, L., Alkmim, F.F., Pedrosa-Soares, A.C., Gonçalves, C.C., Vieira, V., 2018. From the plutonic root to the volcanic roof of a continental magmatic arc: a review of the Neoproterozoic Araçuaí Orogeny, southeastern Brazil. International Journal Earth Science. 107, 337–358. https://doi.org/10.1007/s00531-017-1494-5.
29. Richter, F., Lana, C., Steven, G., Buick, I., Pedrosa-Soares, A.C., Alkmim, F.F., Cutts, K., 2016. Sedimentation, metamorphism and granite generation in a back-arc region: Records from the Ediacaran Nova Venecia Complex (Aracuai Orogeny, Southeastern Brazil). Precambrian Research. 272, 78–100.
30. Santiago, R., Caxito, F.A., Pedrosa-Soares, A.C., Neves, M., Dantas, E.L., 2020. Tonian Island Arc Remnants in the Northern Ribeira Orogeny of Western Gondwana: the Caxixe Batholith (Espírito Santo, SE Brazil). Precambrian Research. p. 105944.
31. Soares, C.C.V., Queiroga, G., Pedrosa-Soares, A.C., Gouvêa, L.P., Valeriano, C.M., Melo, M.G., Marques, R.A., Freitas, R.D.A., 2020. The Ediacaran Rio Doce magmatic arc in the Araçuaí – Ribeira boundary sector, southeast Brazil: lithochemistry and isotopic (Sm–Nd and Sr) signatures. Journal of South American Earth Sciences. 102880 https://doi.org/10.1016/j.jsames.2020.102880.
32. Peixoto, E., Pedrosa-Soares, A.C., Alkmim, F.F., Dussin, I.A., 2015. A suture-related accretionary wedge formed in the Neoproterozoic Araçuaí Orogeny (SE Brazil) during Western Gondwanaland assembly. Gondwana Research. 27, 878–896. https://doi.org/10.1016/j.gr.2013.11.010.
33. Santiago, R., Caxito, F.A., Pedrosa-Soares, A.C., Neves, M., Dantas, E.L., Calegari, S.S., Lana, C. 2023. Records of the accretionary, collisional and post-collisional evolution of western Gondwana in the high grade core of the Araçuaí-Ribeira Orogenyic system, SE Brazil. Precambrian Research. 397, 107191. https://doi.org/10.1016/j.precamres.2023.107191
34. Melo, M.G., Stevens, G., Lana, C., Pedrosa-Soares, A.C., Frei, D., Alkmim, F.F., Alkmin, L. A., 2017a. Two cryptic anatectic events within a syn-collisional granitoid from the Araçuaí Orogeny (southeastern Brazil): evidence from the polymetamorphic Carlos Chagas batholith. Lithos 277, 51–71. https://doi.org/10.1016/j.lithos.2016.10.012.
35. Melo, M.G., Lana, C., Stevens, G., Pedrosa-Soares, A.C., Gerdes, A., Alkmin, L.A., Nalini Jr., H.A., Alkmim, F.F., 2017b. Assessing the isotopic evolution of S-type granites of the Carlos Chagas Batholith, SE Brazil: clues from U–Pb, Hf isotopes, Ti geothermometry and trace element composition of zircon. Lithos 284–285, 730–750. https://doi.org/10.1016/j.lithos.2017.05.025.

36. Serrano, P., Pedrosa-Soares, A., Medeiros-Junior, E., Fonte-Boa, T., Araújo, C., Dussin, I., Queiroga, G., Lana, C., 2018. A-type Medina batholith and post-collisional anatexis in the Araçuaí Orogeny (SE Brazil). Lithos 320–321, 515–536. https://doi.org/10.1016/j.lithos.2018.09.009.
37. Wiedemann-Leonardos, C.M., Medeiros, S.R., Mendes, J.C., Ludka, I.P., Moura, J.C., 2002. The architecture of late Orogenyic plutons in the araçuaí-ribeira folded belt, southeast Brazil. Gondwana Res. 5 (2), 381–399. https://doi.org/10.1016/S1342- 937X(05)70730-9.
38. De Campos, C.P., Mendes, J.C., Ludka, I.P., Medeiros, S.R., Moura, J.C., Wallfass, C., 2004. A review of the Brazilian magmatism in southern Espirito Santo, Brazil, with emphasis on postcollisional magmatism. Journal Virtual Explorer 17, 1–35.
39. Pedrosa-Soares, A.C., Noce, C.M., Wiedemann, C.M., Pinto, C.P., 2001. The Aracuai-West Congo Orogeny in Brazil: An overview of a confined Orogeny formed during Gondwanland assembly. Precambrian Research. 110, 307–323.
40. Medeiros, S.R., Wiedemann, C.M., Vriend, S., 2001. Evidence of mingling between contrasting magmas in a deep plutonic environment: the example of Várzea Alegre in the Panafrican/Brasiliano Mobile Belt in Brazil. Anais da Academia Brasileira de Ciências. 73, 99–119.
41. Mendes, J.C., Medeiros, S.R., McReath, I., De Campos, C.M.P., 2005. Cambro-ordovician magmatism in SE Brazil: U-Pb and Rb-Sr ages, combined with Sr and Nd isotopic data of charnockitic rocks from the Várzea Alegre complex. Gondwana Research. 8, 337–345. https://doi.org/10.1016/S1342-937X(05)71139-4.
42. Mendes, J.C., De Campos, C.M.P., 2012. Norite and charnockites from the Venda Nova Pluton, SE Brazil: intensive parameters and some petrogenetic constraints. Geosciences Frontiers. 3, 789–800. https://doi.org/10.1016/j.gsf.2012.05.009.
43. Bayer, P., Schimidt-Thomé, R., Weber-Diefenbach, K., Horn, H.A. Complex concentric granitoid intrusions in the coastal mobile belt, Espírito Santo, Brazil: The Santa Angélica Pluton—An example. Geol. Rundsch. 1987, 76, 357–371.
44. Schimidt-Thomé, R., Weber-Diefenbach, H., 1987. Evidence for froze-in magma mixing in Brasiliano calc-alkaline intrusions: the Santa Angélica pluton, southern Espírito Santo, Brazil. Rev. Bras. Geociencias 17 (4), 498–506.
45. Aranda, R.O., Chaves, A.O., Medeiros Júnior, E.B., Venturini Junior, R., 2020. Petrology of the Afonso cláudio intrusive complex: new insights for the cambro-ordovician post-collisional magmatism in the araçuaí-west Congo Orogeny, southeast Brazil. Journal of South American Earth Science. 98, 102465 https://doi.org/10.1016/j.jsames.2019.102465.
46. Araujo, C., Pedrosa-Soaresa, A., Lana, C., Dussin, I., Queiroga, G., Serrano, P., Medeiros- Junior, E., 2020. Zircon in emplacement borders of post-collisional plutons compared to country rocks: A study on morphology, internal texture, U Th–Pb geochronology and Hf isotopes (Aracuai Orogeny. SE Brazil). Lithos, 352–353, 105252. https://doi.org/10.1016/j.lithos.2019.105252.
47. Duffles Teixeira, P.A., Fernandes, C.M., Mendes, J.C., Medeiros, S.R., Rocha, I.S.A., 2020. U-Pb LA-ICP-MS and geochemical data of the Alto Chapéu Pluton: contributions on bimodal post-collisional magmatism in the Araçuaí belt (SE Brazil). Journal of South American Earth Science, 103, 102724. https://doi.org/10.1016/j.jsames.2020.102724
48. Melo, M.G., Lana, C., Stevens, G., Hartwig, M.E., Pimenta, M.S., 2020. Deciphering the source of multiple U-Pb ages and complex Hf isotope composition in zircon from post-collisional charnockite-granite associations from the Araçuaí Orogeny (southeastern Brazil). Journal of South American Earth Science, 103, 102792. https://doi.org/10.1016/j.jsames.2020.102792.
49. Bellon, U.D., Souza-Junior, G.F., Temporim, F.A., D'agrella-Filho, M.S., Trindade, R.I.F. 2022. U-Pb geochronology of a reversely zoned pluton: Records of pre-to-post colisional magmatismo of the Araçuaí belt (SE-Brazil)?. Journal of South American Earth Science, V 119 (104045).
50. Potratz, G.L., Geraldes, M.C., Medeiros-Junior, E.B., Temporim, F.A., Martins, M.V.A. 2022. A Juvenile Component in the Pre- and Post-Collisional Magmatism in the Transition Zone between the Araçuaí and Ribeira Orogenys (SE Brazil). Minerals, 12: 1378.
51. Noce C.M., Teixeira W., Quéméneur J.J.G., Martins V.T.S., Bolzachini, E. 2000. Isotopic signatures of Paleoproterozoic granitoids from southern São Francisco Craton, NE Brazil, and implications for the evolution of the Transamazonian Orogeny. Journal of South American Earth Science, 13: 225-239.
52. Martins, V.T.S., Teixeira, W., Noce, C.M., Pedrosa-Soares, A.C., 2004. Sr and Nd characteristics of brasiliano/pan-african granitoid plutons of the Araçuaí Orogeny, southeastern Brazil: tectonic implications. Gondwana Res. 7, 75–89. https://doi.org/ 10.1016/S1342-937X(05)70307-5.
53. Sollner, H.S., Lammerer, B., Wiedemann-Leonardos, C., 2000. Dating the Araçuaí- ribeira mobile belt of Brazil. In: Sonderheft, Zeitschrift (Ed.), Angwandte Geologie, SH1, pp. 245–255.
54. Petitgirard, S., Vauchez, A., Egydio-Silva, M., Bruguier, O., Camps, P., Moni´e, P., Babinsky, M., Mondou, M., 2009. Conflicting structural and geochronological data from the Ibiturana quartz-syenite (SE Brazil): effect of protracted "hot" Orogeny and slow cooling rate? Tectonophysics 477, 174–196. https://doi.org/10.1016/j.tecto.2009.02.039.

55. Baltazar, O.F., Zucchetti, M., Oliveira, S.A.M., Scandolara, J., Silva, L.C., 2010. Geologia das Folhas São Gabriel Da Palha e Linhares. Programa Geologia do Brasil. CPRM–Serviço Geológico do Brasil, Belo Horizonte.
56. Ulbrich, H. H. G. J., Vlach, S. R. F., Janasi, V. A. 2001 O mapeamento faciológico em rochas ígneas plutônicas. Revista Brasileira de Geociências, v. 31, p. 163-172.
57. Jackson, S.E., Pearson, N.J., Griffin, W.L., Belousova, E.A., 2004. Applying laser ablation-inductively coupled plasma-mass spectrometry to in situ U-Pb zircon geochronology. Chem. Geol. 211 (1–2), 47–69. https://doi.org/10.1016/j.chemgeo.2004.06.017.
58. Alves, M.I., Almeida, B.S., Cardoso, L.M.C., Santos, A.C., Appi, C. Bertotti, A.L., Chemale, F., Tavares Jr, A.D., Martons, M.V.A., Geraldes, M.C. 2019 Isotopic Composition of Lu, Hf, and Yb in GJ-1, 91500 and Mud Tank reference materials measured by LA-ICP-MS: Application of the Lu-Hf geochronology in zircon. Journal of Sedimentary Environments 4 (2): 220-248.
59. Streckeisen, A., 1976. To each plutonic rock its proper name. Earth Science Reviews. 12, 1–33. https://doi.org/10.1016/0012-8252(76)90052-0
60. Whitney, D.L., Evans, B.W., 2010. Abbreviations for names of rock-forming minerals. Am. Mineral. 95, 185–187. https://doi.org/10.2138/am.2010.3371.
61. Medeiros, J.D.C., 2013. Caracterização petrográfica e litogeoquímica do Batólito Forno Grande, Castelo, Espírito Santo. Graduation Work Final – Universidade Federal do Espírito Santo, Alegre, p. 96.
62. Meyer, A.P., 2017. Geologia e geoquímica da porção sul do Maciço Castelo-ES. PhD Thesis. Universidade Estadual Paulista, Instituto de Geociências e Ciências Exatas Rio Claro, 143 f.
63. De La Roche, H., Leterrier, J., Grande Claude, P., Marchal, M., 1980. A volcanic and plutonics rocks classification using R1–R2 diagrams and major element analyses – Its relationships and current nomenclature. Chemical Geology. 29, 183–221.
64. Boynton, W.V., 1984. Cosmochemistry of the rare earth elements, meteorite studies. In: Henderson, P. (Ed.), Rare Earth Element Geochemistry, vol. 1. Elsevier, Amsterdam, pp. 63–114.
65. Sun, S.S., McDonough, W.F., 1989. Chemical and isotopic systematics of oceanic basalts: implications for mantle composition and processes. In: Saunders, A.D., Norry, M. (Eds.), Magmatism in Ocean Basins, vol. 42. Geological Society of London Special Publications, pp. 313–345. https://doi.org/10.1144/GSL.SP.1989.042.01.19.
66. Frost, B.R., Frost, C.D., 2008. A Geochemical classification for feldspathic igneous rocks. J. Petrol. 49, 1955–1969.
67. Hollocher, K., Robinson, P., Walsh, E., and Roberts, D. 2012, Geochemistry of amphibolite-facies volcanic and gabbros of the Støren nappe in extensions west and southwest of Trondheim, Western Gneiss Region, Norway: A key to correlations and paleotectonic settings: American Journal of Science, v. 312, p. 357–416, https://doi.org /10.2475/04.2012.01.
68. Silva, J. N. DA (Org). 1992. Programa levantamentos geológicos básicos do Brasil. Cachoeiro de Itapemirim. Folha SF.24-V-A-V. Estado do Espírito Santo. Escala 1:100.000., DNPM/CPRM.
69. Vieira, V.S., Menezes, R.G., Orgs, 2015. Geologia e Recursos Minerais do Estado do Estado do Espírito Santo: texto explicativo do mapa geológico e de recursos minerais, escala 1:400.000. In: Programa Geologia Do Brasil, CPRM - Serviço Geológico Do Brasil, Belo Horizonte.
70. Zhang, J., Wang, T., Castro, A., Zhang, L., Shi, X., Thong, Y., Zhang, Z., Guo, L., Yang, Q., Iaccheri, L, M. 2016. Multiple Mixing and Hybridization from Magma Source to Final Emplacement in the Permian Yamatu Pluton, the Northern Alxa Block, China. Journal of Petrology, 2016, Vol. 57, No. 5, 933–980.
71. Grogan, S.E., Reavy, R.J. 2002. Disequilibrium textures in the Leinster Granite Complex, SE Ireland: evidence for acid-acid magma mixing. Mineralogical Magazine, Vol. 66(6), pp. 929–939.
72. Alves, A., Janasi, V.A., Pereira, G.S., Prado, F.A., Munoz, P.R.M. 2021. Unravelling the hidden evidences of magma mixing processes via combination of in situ Sr isotopes and trace elements analyses on plagioclase crystals. Lithos, 404-405 (106435).
73. Sousa, C.S., Conceição, H., Soares, H.S., Fernandes, D.M., Rosa, M.L.S. 2022. Magmatic processes recorded in plagioclase crystals of the Rio Jacaré Batholith, Sergipano Orogenyic System, Northeast Brazil. Journal of South American Earth Sciences, 118 (103942).
74. Hibbard, M.J., 1995. Petrography to Petrogenesis. Prentice Hall, Englewood Cliffs, New Jersey, p. 587p.
75. Vernon, R. H. 1983. Restitc, xenoliths and microgranitoid enclaves in granites. Journal and Proceedings of the Royal Society of New South Walts, 116: 77-103.
76. Barbarin, B., 2005. Mafic magmatic enclaves and mafic rocks associated with some granitoids of the central Sierra Nevada batholith, California: nature, origin, and relations with the hosts. Lithos 80, 155–177.
77. Barbarin, B., Didier, J., 1992. Genesis and evolution of mafic microgranular enclaves through various types of interaction between coexisting felsic and mafic magmas. Earth Environments Science Transact. Royal Society Edinburgh 83, 145–153.
78. Zorpi, M.J., Coulon, C., Orsini, J.B., Cocirta, C., 1989. Magma mingling, zoning and emplacement in calc-alkaline granitoid plutons. Tectonophysics 157, 315–329

79. Vernon, R.H.1984. Microgranitoid enclaves in granites: Globules of hybrid magma quenched in a plutonic environment: Nature, v. 309, p. 438–439.
80. Vernon, R.H. 1991. Crystallization and hybridism in micro granitoid enclave magmas: Microstructural evidence: Journal of Geophysical Research, v. 95, p. 17, 849–17, 859.
81. Chappell, B. W., White, A. J. R., Wyborn, D. 1987. The importance of residual source material (restite) in granite petrogenesis. Journal of Petrology, 28, 1111-38
82. Chappell, B.W., White, A.J.R., 1992. I-type and S-type granites in the Lachlan Fold Belt. Transactions of the Royal Society of Edinburgh: Earth Sciences 83, 1–26.
83. Zhang, S. H., Zhao, Y. 2017. Cogenetic origin of mafic microgranular enclaves in calc-alkaline granitoids: The Permian plutons in the northern North China Block. Geosphere, v. 13, no. 2, p. 482–517.
84. Flood, R.H., Vernon, R.H. 1988. Microstructural evidence of orders of crystallization in granitoid rocks. Lithos, 21, 237-245.
85. Elangovan, R., Krishna, K., Vishwakarma, N., Hari, K. R., and Mohan, M. R. (2017). Interaction of coeval felsic and mafic magmas from the Kanker granite, Pithora region, Bastar Craton, Central India. J. Earth Syst. Sci. 126:92. doi: 10.1007/s12040-017-0886-z.
86. Slaby, E., Gotze, J., Worner, G., Simon, K., Wrzalik, R., Smigielski, M., 2008. K-feldspar phenocrysts in microgranular magmatic enclaves: cathodoluminescence and geochemical study of crystal growth as a marker of magma mingling dynamics. Lithos 105, 85–97. https://doi.org/10.1016/j.lithos.2008.02.006.
87. Renjith, ML., Charan, S.N., Subbarao, D.V., Babu, E.V.S.S.K., Rajashekhar, V.B. 2014. Grain to outcrop-scale frozen moments of dynamic magma mixing in the syenite magma chamber, Yelagiri Alkaline Complex, South India. Geoscience Frontiers, (5) 801-820.
88. Kumar, S., Rino, V., Pal, A.B. 2004. Field evidence of magma mixing from microgranular enclaves hosted in Palaeoproterozoic Malanjkhand granitoids, central India. Gondwana Research, 7(2), 539-548.
89. Marshall, L.A., Sparks, R. S. J. 1984. Origin of some mixed-magma and net-veined ring intrusions. Journal of the Geological Society, 141 (1): 171–182. doi: https://doi.org/10.1144/gsjgs.141.1.0171
90. Hibbard, M.J.1981. The magma mixing origin of mantled feldspars: Contributions to Mineralogy and Petrology, v. 76, p. 158–170.
91. Barbarin, B. 1990. Plagioclase xenocrysts and mafic magmatic enclaves in some granitoids of the Sierra Nevada batholith, California. Journal of Geophysical Research, v. 95, p. 17.747–17.756.
92. Janoušek, V., Braithwaite, C.J.R., Bowes, D.R., Gerdes, A. 2004. Magma-mixing in the genesis of Hercynian calc-alkaline granitoids: an integrated petrographic and geochemical study of the Sávaza intrusion, Central Bohemian Pluton, Czech Republic. Lithos, 78, 67–99.
93. Dománska-Siuda, J., Słaby, E., Szuszkiewicz, A., 2019. Ambiguous isotopic and geochemical signatures resulting from limited melt interactions in a seemingly composite pluton: a case study from the Strzegom–Sobótka Massif (Sudetes, Poland). Int. J. Earth Sci. 108, 931–962. https://doi.org/10.1007/s00531-019-01687-w.
94. Baxter, S., Feely, M., 2002. Magma mixing and mingling textures in granitoids: examples from the Galway Granite, Connemara, Ireland. Mineral. Petrol. 76, 63–74. https:// doi.org/10.1007/s007100200032.
95. Perugini, D., Poli, G. 2005. Viscous fingering during replenishment of felsic magma chambers by continuous inputs of mafic magmas: field evidence and fluid-mechanics experiments. Geology 33:5–8
96. Perugini, D., De Campos, C.P., Dingwell, D.B., Petrelli, M., Poli, G. 2008. Trace element mobility during magma mixing: preliminary experimental results. Chem Geol 256:146–157.
97. Petrelli, M., Perugini, D., Poli, G. 2011. Transition to Chaos and implications for Time-scales of Magma Hybridization during mixing processes in Magma chambers. Lithos 125:211–220.
98. Morgavi, D., Perugini, D., De Campos, C.P., Ertl-Ingrisch, W., Dingwell, D.B. 2013. Time evolution of chemical exchanges during mixing of rhyolitic and basaltic melts. Contrib Mineral Petrology, 166(2):615–638.
99. De Campos, C.P., Perugini, D., Ertel-Ingrisch, W., Dingwell, D.B., Poli, G. 2011. Enhancement of Magma mixing efficiency by Chaotic Dynamics: an experimental study. Contrib Mineral Petr 161:863–88.
100. Kemp, A.I.S., Hawkesworth, C.J., Foster, G.L., Paterson, B.A., Woodhead, J.D., Hergt, J. M., Gray, C.M., Whitehouse, M.J., 2007. Magmatic and crustal differentiation history of granitic rocks from Hf-O isotopes in zircon. Science 315, 980–983. https://doi.org/10.1126/science.1136154.
101. Miller, J.S., Matzel, J.E.P., Miller, C.F., Burgess, S.D., Miller, R.B., 2007. Zircon growth and recycling during the assembly of large, composite arc plutons. J. Volcanol. Geoth. Res. 167, 282–299. https://doi.org/10.1016/j.jvolgeores.2007.04.019.
102. Mendes, J.C., Wiedemann, C.M., McReath, I., 2002. Norito e Charnoenderbitos da Borda do Maciço Intrusivo de Venda Nova, Espírito Santo, vol. 25. Anuário do Instituto de Geociências, pp. 99–124.
103. Onken, C. T., Eberhard-Schmid, J., Hauser, L., Marioni, S., Galli, A., Janasi, V. A., & Schmidt, M. W. 2024: Timing and origin of the post-collisional Venda Nova and Várzea Alegre Plutons from the Araçuaí belt, Espírito Santo, Brazil. Lithos, 107677. https://doi.org/10.1016/j.lithos.2024.107677.

 doi:10.20944/preprints202411.0370.v1



104. Noce, C.M., Pedrosa-Soares, A.C., Silva, L.C., Armstrong, R., Piuzana, D. 2007. Evolution of polycyclic basement complexes in the Araçuaí Orogeny, based on U-Pb SHRIMP data: Implications for Brazil-Africa links in Paleoproterozoic time. Precambrian Res. 159, 60–78. https://doi.org/10.1016/j.precamres.2007.06.001.
105. Lana, C., Mazoz, A., Narduzzi, F., Cutts, K., Fonseca, M., 2020. Paleoproterozoic sources for Cordilleran-type Neoproterozoic granitoids from the Araçuaí Orogeny (SE Brazil): constraints from Hf isotope zircon composition. Lithos, 105815. https://doi.org/10.1016/j.lithos.2020.105815.
106. Pereira, V.H., Mendes, J., Carvalho, M., Coelho, V., Medeiros, S., Valeriano, C. 2023. Petrogenesis of Estrela is granitoid and implications for the evolution of the Rio Doce magmatic arc: Araçuaí-Ribeira Orogenyic system, SE Brazil. 126.104337.10.1016/j.jsames.2023.104337.
107. Peixoto, C.A., Heilbron, M., Ragatky, D., Armstrong, R., Dantas, E., Valeriano, C.M., Simonetti, A., 2017. Tectonic evolution of the Juvenile Tonian Serra da Prata magmatic arc in the Ribeira belt, SE Brazil: implications for early West Gondwana amalgamation. Precambrian Res. 302, 221–254. https://doi.org/10.1016/j. precamres.2017.09.017.